Paleoceanography and Paleoclimatology

RESEARCH ARTICLE
10.1029/2022PA004517

**Key Points:**

- Deeper palustrine and unaltered lacustrine carbonates record warm season water temperatures of approximately 41 and 38°C, respectively
- High temperatures from well-preserved shallower palustrine carbonates likely reflect radiative heating
- Careful facies analysis is imperative for robust paleoclimate interpretation of heterogeneous terrestrial carbonate archives

**Supporting Information:**

Supporting Information may be found in the online version of this article.

**Correspondence to:**

A. C. Fetrow,
anne.fetrow@colorado.edu

**Citation:**

Fetrow, A. C., Snell, K. E., Di Fiori, R. V., Long, S. P., & Bonde, J. W. (2022). How hot is too hot? Disentangling mid-Cretaceous hothouse paleoclimate from diagenesis. *Paleoceanography and Paleoclimatology*, *37*, e2022PA004517. https://doi.org/10.1029/2022PA004517

Received 18 JUL 2022
Accepted 9 NOV 2022

**Author Contributions:**

**Conceptualization:** K. E. Snell, S. P. Long, J. W. Bonde
**Data curation:** A. C. Fetrow
**Formal analysis:** A. C. Fetrow
**Funding acquisition:** K. E. Snell, S. P. Long, J. W. Bonde
**Investigation:** A. C. Fetrow, K. E. Snell, R. V. Di Fiori, S. P. Long, J. W. Bonde
**Methodology:** A. C. Fetrow, K. E. Snell
**Project Administration:** A. C. Fetrow, K. E. Snell
**Resources:** A. C. Fetrow
**Software:** A. C. Fetrow, K. E. Snell
**Supervision:** K. E. Snell
**Validation:** A. C. Fetrow
**Visualization:** A. C. Fetrow, R. V. Di Fiori
**Writing – original draft:** A. C. Fetrow, R. V. Di Fiori



# How Hot Is Too Hot? Disentangling Mid-Cretaceous Hothouse Paleoclimate From Diagenesis

**A. C. Fetrow[1], K. E. Snell[1], R. V. Di Fiori[2], S. P. Long[3], and J. W. Bonde[4]**

[1]University of Colorado Boulder, Boulder, CO, USA, [2]Idaho Geological Survey, University of Idaho, Moscow, ID, USA, [3]Washington State University, Pullman, WA, USA, [4]Nevada State Museum, Carson City, NV, USA

**Abstract** The North American Newark Canyon Formation (NCF; ~113–98 Ma) presents an opportunity to examine how terrestrial carbonate facies reflect different aspects of paleoclimate during one of the hottest periods of Earth's history. The lower NCF type section preserves heterogeneous palustrine facies and the upper NCF preserves lacustrine deposits. We combined carbonate facies analysis with $\delta^{13}C$, $\delta^{18}O$, and $\Delta_{47}$ data sets to assess which carbonate facies preserve stable isotope signals that are most representative of climatic conditions. Palustrine facies record the heterogeneity of the original wetland environment in which they formed. Using the pelmicrite facies that formed in deeper wetlands, we interpret a lower temperature zone (35–40°C) to reflect warm season water temperatures. In contrast, a mottled micrite facies which formed in shallower wetlands records hotter temperatures (36–68°C). These hotter temperatures reflect radiatively heated "bare-skin" temperatures that occurred in a shallow depositional setting. The lower lacustrine unit has been secondarily altered by hydrothermal fluids while the upper lacustrine unit likely preserves primary temperatures and $\delta^{18}O_{water}$ of catchment-integrated precipitation. Resultantly, the palustrine pelmicrite and lacustrine micrite are the facies most likely to reflect ambient climate conditions, and therefore, are the best facies to use for paleoclimate interpretations. Average warm season water temperatures of 41.1 ± 3.6°C and 37.8 ± 2.5°C are preserved by the palustrine pelmicrite (~113–112 Ma) and lacustrine micrite (~112–103 Ma), respectively. These data support previous interpretations of the mid-Cretaceous as a hothouse climate and demonstrate the importance of characterizing facies for identifying the data most representative of past climates.

**Plain Language Summary** Considered a "supergreenhouse" world, the Cretaceous (145–65 Mya) was one of the hottest periods in geologic history. Understanding how environments respond to extreme global warmth provides insights that will help to mitigate the harmful effects of modern climate change. Geochemical signals, like stable isotopes, preserved in rocks allow us to reconstruct past climate conditions. We use stable isotope geochemistry on limestones (rocks made of carbonate minerals) to estimate average mid-Cretaceous (~110 Mya) summer temperatures in Nevada, USA. We examine limestones that formed in wetlands and lakes to assess which types record signals representative of the original landscape and which have values that were altered after the rock formed. We find that carbonates deposited in the shallowest parts of wetland environments record temperatures much hotter than air or deeper water temperatures due to extreme land surface heating, while deeper wetland limestones preserve temperatures more representative of ambient conditions. Average warm season water temperatures for wetland and lake carbonates are approximately 41 and 38°C, respectively, revealing hot conditions that support our understanding of the Cretaceous as a greenhouse world. This research provides an example of how to interpret useful climate information from complex carbonate data sets.

## 1. Introduction

The Cretaceous was a time of highly active tectonism, including the ongoing breakup of supercontinent Pangaea and increased seafloor spreading rates, as well as of greenhouse climate, including elevated global temperatures and a reduced equator-to-poles temperature gradient (Forster et al., 2007; B. T. Huber et al., 2002; M. Huber, 2008; Pagani et al., 2013; Takashima et al., 2006). The mid-Cretaceous (~113–89 Ma) marks particular warmth, evolving from a "warm greenhouse" to a "hot greenhouse," during the Cretaceous Thermal Maximum (~95–90 Ma; Forster et al., 2007; B. T. Huber et al., 2018). Much more is known about the response of marine environments during this time than terrestrial environments. Terrestrial carbonates offer potential archives through which to examine the past climatic, hydrologic, environmental, and surface elevation conditions using a variety of proxy tools, such as stable isotopes (i.e., $\delta^{13}C$, $\delta^{18}O$, and $\Delta_{47}$). Lacustrine and pedogenic carbonates have been used

**Writing – review & editing:** A. C. Fetrow, K. E. Snell, R. V. Di Fiori, S. P. Long, J. W. Bonde

extensively as paleoclimate archives (e.g., Gierlowski-Kordesch, 2010; Ingalls et al., 2022; Passey et al., 2010; Petersen et al., 2019; Quade et al., 2013; Snell et al., 2013), while palustrine (i.e., wetland) carbonates have not.

Palustrine deposits are common in the terrestrial rock record, especially in warm and humid periods of geologic history such as the mid-Miocene, Eocene, and Cretaceous (Alonso-Zarza & Wright, 2010; Freytet & Verrecchia, 2002; Platt, 1989). They represent a depositional spectrum between open water (i.e., lacustrine) and subaerially exposure (i.e., pedogenic) of the landscape (Alonso-Zarza, 2003; Alonso-Zarza & Wright, 2010; Arenas-Abad et al., 2010). As a result, palustrine rocks exhibit characteristics of both ends of this depositional spectrum, requiring interpretation as a distinctive depositional setting from lacustrine and pedogenic environments. Therefore, to understand how past terrestrial environments respond spatially and temporally to different climate states, we must understand how each of these archives encode environmental signals and consider the heterogeneity that exists within the same depositional system and/or proxy archive. For instance, carbonate clumped isotopes temperature estimates ($T(\Delta_{47})$) record the temperature at which the carbonate mineral precipitated, so we must understand the drivers of mineral formation to accurately interpret what $T(\Delta_{47})$ values represent (e.g., a specific depositional setting, a particular season, or extreme conditions on spatial and temporal scales). By integrating stable isotope records with detailed depositional models, we can account for the natural variability of environmental conditions, and separate the signal of a heterogeneous primary depositional landscape from post-depositional alteration.

We studied the sedimentology and stable isotope geochemistry of the North American Newark Canyon Formation (NCF; ~113–98 Ma) to better understand how continental interiors responded to the globally hot conditions of the mid-Cretaceous, and to improve our understanding of how palustrine and lacustrine environments capture paleoclimate and paleoenvironmental signals during a period of unique climatic history. The NCF type section preserves a sequence of palustrine, fluvial, and lacustrine sediments. Using facies analysis, optical and cathodoluminescence (CL) microscopy, X-ray diffraction (XRD), and stable isotope geochemistry ($\delta^{13}C_{carb}$, $\delta^{18}O_{carb}$, $\delta^{18}O_{water}$, and $\Delta_{47}$ temperatures (i.e., $T(\Delta_{47})$), we assessed which palustrine and lacustrine facies preserve unaltered stable isotope proxy signals that are also most representative of climatic and environmental conditions of the depositional landscape. Finally, we evaluated the paleoclimatic and paleoenvironmental conditions in the Sevier Hinterland region of southwestern North America during the mid-Cretaceous (Figure 1).

## 2. Background

### 2.1. Overview of Cretaceous Climate

During the mid-Cretaceous, defined here as the Albian to Turonian (~113–89 Ma), global climate evolved from a "warm greenhouse" to a "hot greenhouse" at the Cretaceous Thermal Maximum, reaching an apex of warmth during the early to mid-Turonian (Forster et al., 2007; B. T. Huber et al., 2018). Globally averaged surface temperatures were estimated to have been 6–12°C warmer than pre-industrial conditions (Barron, 1983; Barron et al., 1993; Barron & Washington, 1982; Gale, 2000; B. T. Huber et al., 2002). Key features of Cretaceous climate include much warmer temperatures at polar latitudes than today, a reduced equator to pole temperature gradient (Barron et al., 1993; Barron & Washington, 1982, 1984; B. T. Huber et al., 1995; Ludvigson et al., 2015; Poulsen et al., 1999), and regional changes to seasonal range of temperature (Fluteau et al., 2007). On land, frost-intolerant vertebrate and plant assemblages suggest that mean annual temperatures (MATs) at polar latitudes were much warmer than today in both hemispheres during the Cretaceous, with winter temperatures above freezing (Brouwers et al., 1987; Case et al., 2000; Olivero et al., 1991; J. M. Parrish et al., 1987; J. T. Parrish & Spicer, 1988; Rich et al., 2002; Tarduno et al., 1998). $\delta^{18}O$ values from northern European brachiopods indicate mid-latitude temperatures rose ~6–7°C during the latest Cenomanian, reached a maximum at the Cenomanian-Turonian boundary (93 Ma), and continued to increase into the mid-Turonian (Jenkyns, 2010; Voigt et al., 2006). $T(\Delta_{47})$ estimates from mid-Cretaceous oyster fossils suggest that shallow surface waters of the North American Western Interior Seaway (WIS) were as hot as modern tropical temperatures (28–34°C; Jones et al., 2022). North American mid-latitude terrestrial sites preserve elevated mean annual and mean warm season temperatures during the mid-Cretaceous (Gröcke et al., 1999; Ludvigson et al., 2010, 2015; C. A. Suarez et al., 2014; M. B. Suarez et al., 2021). For example, mid-Cretaceous $T(\Delta_{47})$ estimates from the Cedar Mountain Formation (Utah, USA) range from 30 to 39°C (Ludvigson et al., 2010, 2015; M. B. Suarez et al., 2021). These estimates were derived from paleosol and palustrine carbonates and are interpreted to record warm season biased soil temperatures and/or the potential effects of direct solar radiation.

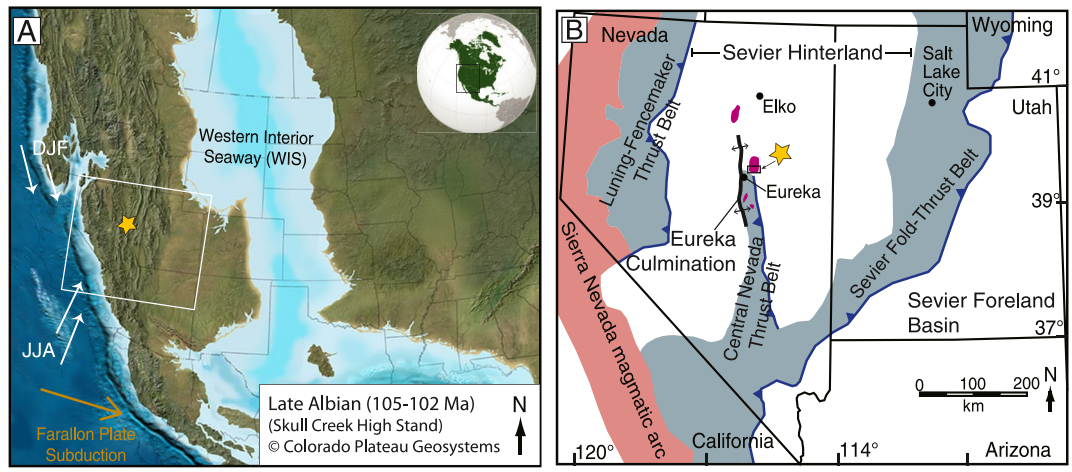


**Figure 1.** The yellow star in both maps represents the approximate site of deposition of the Newark Canyon Formation (NCF) type section. (a) Reconstruction map of southern North America during the late Albian (~105–102 Ma; modified from Blakey, 2020). Modeled seasonal prevailing wind directions are shown for Albian (~100 Ma) winter (DJF: December, January, February) and summer (JJA: June, July, August) months with white arrows (Elder, 1988; Poulsen et al., 1999). Dark orange arrow shows approximate direction of subduction of the Farallon plate (DeCelles, 2004; DeCelles & Graham, 2015). The white box indicates the area of the map shown in (b) Regional tectonic map adapted from Di Fiori et al. (2020); Long, Henry, Muntean, Edmondo, and Cassel (2014), and Long, Henry, Muntean, Edmondo, and Thomas (2014). Gray shading shows the approximate spatial extents of Jurassic-Cretaceous deformational provinces of the North American Cordilleran mountain belt in western United States, while pink shading marks the Sierra Nevada magmatic arc (from Van Buer et al., 2009). All mapped NCF depositional basins are shown in purple (from Di Fiori et al., 2021).

Warm Cretaceous climate likely invigorated the hydrologic cycle, meaning that there was increased equator to pole vapor transport that generated more precipitation in wet regions and the aridification of dry regions (Barron & Washington, 1982; Held & Soden, 2002, 2006; Ufnar et al., 2004). This invigoration would have resulted in both elevated surface temperatures and increased humidity due an increase in the volume of water stored in groundwater reservoirs and terrestrial water bodies (e.g., lakes and wetland systems) (Föllmi, 2012; Hay et al., 2018; Wendler & Wendler, 2016). In the western US, paleo-precipitation reconstructions from Albian-Cenomanian paleosol profiles suggest that climate at ~30°N paleolatitude in north-central Texas and southern Oklahoma during the Cretaceous was significantly wetter than today, with precipitation amounts similar to modern tropical climates (Andrzejewski & Tabor, 2020). Similarly, stable isotope mass-balance modeling of meteoric $\delta^{18}O$ values from North American paleosol siderites from the Cenomanian show significantly higher precipitation rates than present day for mid-latitude sites (40°–60°N) (Albian: 2,200 mm/yr at 45°N; Cenomanian: 3,600 mm/yr at 45°N; Ufnar et al., 2008). Paleo-precipitation estimates from the Cedar Mountain Formation, deposited in the Sevier foreland basin ~500 km east of NCF DeCelles & Coogan, 2006; Long, 2019), yielded paleo-precipitation estimates of 735–1,042 mm/yr (M. B. Suarez et al., 2021).

## 2.2. Geologic Background of the NCF

### 2.2.1. Tectonic Setting and Age of the NCF

Subduction of oceanic plates of the Pacific realm under the western margin of the North American continental plate took place from the Jurassic to the Paleogene, giving rise to contractional deformation that thickened the crust, and built the vast North American Cordilleran mountain belt (Burchfiel et al., 1992; DeCelles, 2004; DeCelles & Coogan, 2006; Dewey & Bird, 1970; Dickinson, 2004; Jordan & Allmendinger, 1986; Yonkee & Weil, 2015). The area where the NCF was deposited is part of the broader Sevier hinterland, which is flanked by the Sierra Nevada magmatic arc to the west and the Sevier fold-thrust belt to the east (Figure 1; DeCelles, 2004; DeCelles & Coogan, 2006; Long, Henry, Muntean, Edmondo, & Cassel, 2014; Long, Henry, Muntean, Edmondo, & Thomas, 2014; Wells et al., 2012).

The NCF was deposited in a series of spatially isolated piggyback basins that are distributed along a narrow, ~150 km long, N-S-trending region of central Nevada following the Central Nevada thrust belt (Figure 1; Di

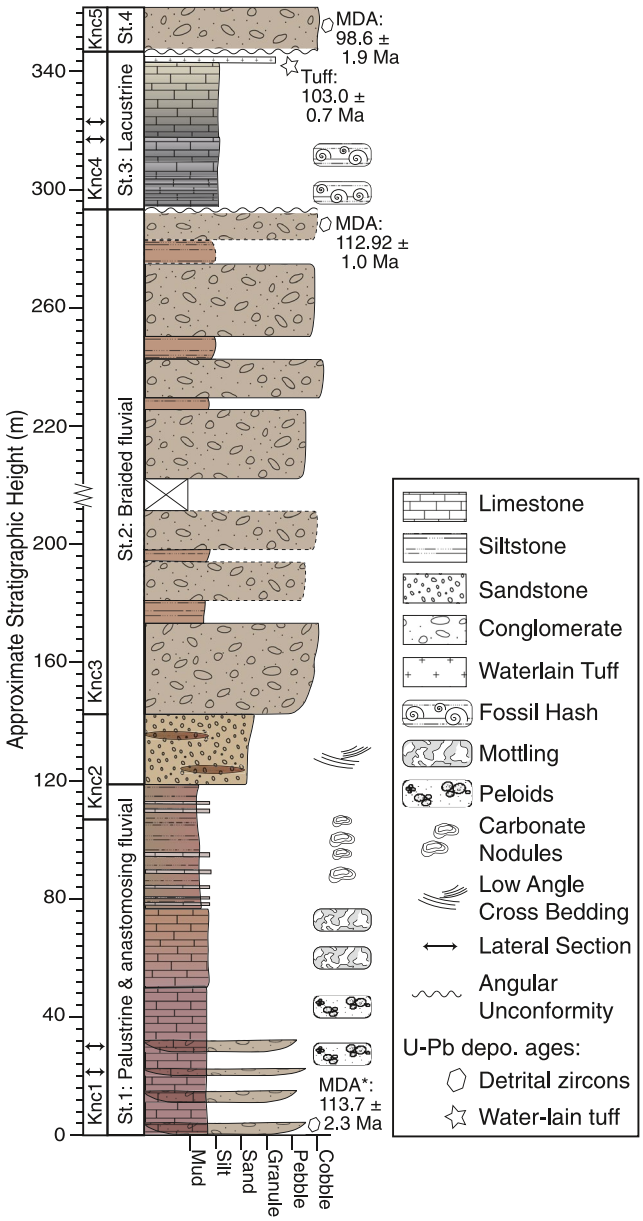


**Figure 2.** Composite stratigraphic column (meters) of the Newark Canyon Formation (NCF) type section with published age constraints (Di Fiori et al., 2020), integrating stratigraphic and lithologic information from the five measured sections to show general basin architecture. Samples were assigned stratigraphic heights from this composite stratigraphic column. The four small double-ended arrows indicate the stratigraphic heights of the lateral sections that were measured (21.5, 30, 317, and 323 m). There is an angular unconformity between the lacustrine unit (Knc4, Stage 3) and the capping conglomerate (Knc5, Stage 4). A U-Pb depositional age from a water-lain tuff (star) and three maximum depositional ages (MDAs) from detrital zircons (hexagons) are shown to the right of the stratigraphic column (Di Fiori et al., 2020). *Note: the MDA used for the base of the section is from a basal mudstone sample located 10 km north of the type section.

Fiori et al., 2021; Long, Henry, Muntean, Edmondo, & Cassel, 2014; Long, Henry, Muntean, Edmondo, & Thomas, 2014; Nolan & Hunt, 1962; Nolan et al., 1974, 1956). Sedimentation in the NCF type section basin is attributed to erosion of the eastern flank of the Eureka Culmination, a structural high of the Central Nevada Thrust belt (Figure 1), based on clast and cross-bedding orientations from the NCF type section that indicate an east-flowing fluvial system (Di Fiori et al., 2020, 2021; Fetrow et al., 2020; Long, 2012, 2015; Long, Henry, Muntean, Edmondo, & Cassel, 2014; Long, Henry, Muntean, Edmondo, & Thomas, 2014; Long et al., 2015; Vandervoort & Schmitt, 1990). An estimated 1.1° ± 3.0° (positive northward) apparent latitude shift for the mid-Cretaceous Sierra Nevada (~100–83 Ma) and negligible apparent rotation of 0.0° ± 4.7° (Hillhouse & Grommé, 2011) indicate that the NCF was deposited at approximately the same latitude as its current position (~39°N).

Di Fiori et al. (2020) divide the NCF type section exposure into five units (Knc1– Knc5). The NCF type section unconformably overlies either the Permian Carbon Ridge Formation, which is composed of marine shelf carbonates, siltstones, conglomerates, or the Mississippian shallow marine Ely Limestone (Druschke et al., 2011; Nolan & Hunt, 1962; Nolan et al., 1956; Strawson, 1981; Vandervoort, 1987). These units stack conformably except for two notable exceptions. First, there is a set of progressive unconformities within Knc3 conglomerate beds, and an angular unconformity at the base of Knc5 that represents ~10 Myr of a depositional hiatus and/or erosion between Knc4 and Knc5 (Di Fiori et al., 2020). The NCF is unconformably overlain by Paleogene volcanics and megabreccias.

Based on the presence of Early Cretaceous freshwater unionids, gastropods, ostracods, and fish fossils, as well as charophytes and other plant macrofossils, the depositional age of the NCF type section exposure was originally estimated to be Aptian-Albian (ca. 126–100 Ma; David, 1941; Fouch et al., 1979; MacNeil, 1939; Nolan et al., 1956; Smith & Ketner, 1976). The faunal list from the NCF exposures across central Nevada now includes a turtle genus *Glyptops*, a member of the freshwater shark family *Hybodontidae*, a gar fish (*Lepisosteidae*), two types of crocodilians, and a number of dinosaur families, which expands the age of some exposures of the NCF further back in the Early Cretaceous (Bonde et al., 2015). U-Pb zircon geochronology from a water-lain tuff yielded a concordia age of a coherent population of zircons at 103.0 ± 0.7 Ma for the top of the NCF type section (Figure 2; Di Fiori et al., 2020). Additionally, U-Pb geochronology of detrital zircons measured using laser ablation-inductively coupled plasma mass spectrometry (LA-ICP-MS) yielded maximum depositional age (MDA) estimates for different units of the type section of 113.7 ± 2.3, 112.92 ± 1.0, 98.6 ± 1.9 Ma (Di Fiori et al., 2020). The113.7 ± 2.3 Ma MDA was from a basal mudstone sample located ~10 km north of the type section, in the Hildebrand exposure of the NCF (Di Fiori et al., 2020).

### 2.2.2. Carbonate-Bearing Facies of the NCF Type Section

Here, we summarize the key depositional environments and associated facies (Table 1) in the NCF type section. Refer to the supplemental materials for addition detail and representative images of each facies. An in-depth explanation of the facies preserved in the NCF is presented in Fetrow et al. (2020). The abbreviation convention used in this study first denotes the rock type using the Folk classification system (Folk, 1959, 1962), and then the interpreted depositional environment is given in the subscript. Knc1-Kn5 correspond to four depositional stages (Stage 1–4 of Fetrow et al., 2020; Figure 2). Stage 1 was dominated by deposition within an anastomosing river floodplain

**Table 1**
*NCF Carbonate-Bearing Facies Description and Abbreviation Reference Guide*

| NCF section | Facies | Depositional setting | Abbreviation |
|---|---|---|---|
| Upper | Micrite | Lacustrine | $M_{(lake)}$ |
| | Biomicrite | Lacustrine | $Mb_{(lake)}$ |
| | Calcareous mudstone | Lacustrine | $Fc_{(lake)}$ |
| Lower | Carbonate nodule | Floodplain soil | $Mn_{(soil)}$ |
| | Biomicrite | Pond | $Mb_{(pond)}$ |
| | Mottled micrite | Palustrine | $Mm_{(wetland)}$ |
| | Pebbly pelmicrite | Palustrine | $Mp_{(wetland)}$ |
| | Calcareous conglomerate | River channel | $Gc_{(channel)}$ |

*Note.* For further detail, refer to the Supporting Information or Fetrow et al. (2020).

where active channels were separated by interchannel topographic lows in which heterogeneous, seasonally ephemeral palustrine environments formed (Figure 3). Depending on proximity to active channels, these wetland environments experienced variable frequencies and quantities of inundation and input of siliciclastic clast material (pebbly conglomerate facies, $Gc_{(channel)}$). Because of these highly variable flooding events, different portions of the wetlands experienced a spectrum of water depths, represented by different facies: areas that likely remained fully submerged (pebbly pelmicrite facies, $Mp_{(wetland)}$), to shallow water areas that experienced more frequent subaerial exposure and desiccation (mottled micrite facies, $Mm_{(wetland)}$), to areas that may have experienced long-duration subaerial exposure that allowed for well-developed pedogenesis (carbonate nodule-bearing paleosol facies, $Mn_{(soil)}$). Farther from the active anastomosing channels, and therefore subject to less frequent inundation events, ponds formed in abandoned channels and slowly filled with allochthonous siliciclastic and autochthonous carbonate sediment (pond biomicrite facies, $Mb_{(pond)}$). These infilled ponds in the channel-distal portions of the river plain underwent minimal weak pedogenesis (e.g., paleosol facies, $Mn_{(soil)}$). The highly variable conditions of the anastomosing river system caused frequent lateral facies shifts that created complex vertical arrangements of these facies within Stage 1 of the type section.

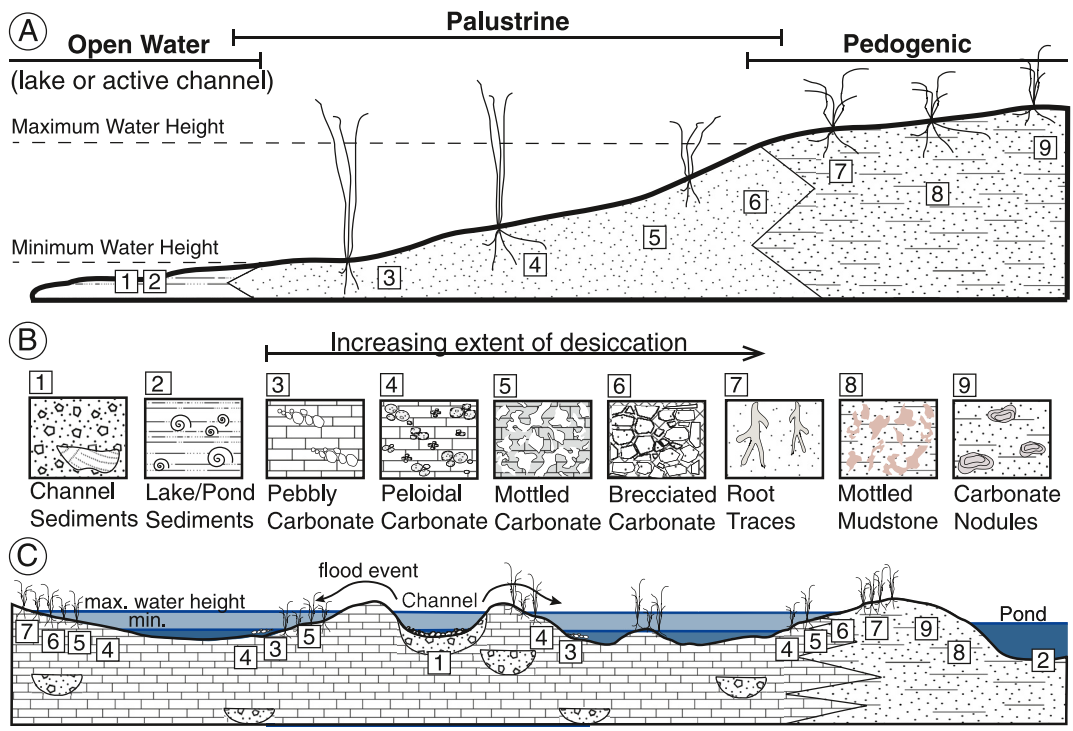


**Figure 3.** (a) Generalized cross-section depositional model for a palustrine environment that spans across open water (e.g., a pond/lake or active fluvial channel) through a palustrine transitional zone to a pedogenic system (modified from Alonso-Zarza, 2003). The fluctuation of surface water in the palustrine zone between a minimum and maximum height creates a spectrum of heterogeneous depositional features. (b) Numbers refer to a spectrum of common depositional features and textures found in carbonate-bearing systems. Some portions of the landscape remain subaqueous while others experience periodic oscillations in the height of surface water, and therefore, are subject to heterogeneous quantities and extents of desiccation, reworking, and overprinting by pedogenic processes. (c) Depositional model for the palustrine facies preserved in Stage 1 of the Newark Canyon Formation type section. Numbers refer to panel (b) and provide examples of where depositional features and facies can form along the palustrine landscape. Periodic inundations created a highly variable palustrine system between active river channels.

A braided river system dominated deposition during Stage 2, preserving bedded pebbly to cobble conglomerates and planar-bedded sandstones, and was likely caused by an increase in structural uplift along the nearby Eureka Culmination that increased sediment supply and the fluvial gradient in the NCF basin (Fetrow et al., 2020). Stage 2 does not preserve any carbonate-bearing facies. Stage 3 was marked by a large-scale, freshwater, balance-filled lacustrine system that indicates either a reorganization of drainage patterns due to new structural containment or an increase in accommodation potentially due to subsidence in the piggyback basin while the sediment supply remained relatively constant (Fetrow et al., 2020). Lacustrine mudstones (calcareous mudstone facies, $Fc_{(lake)}$), biomicrites containing abundant fossil hash (biomicrite, $Mb_{(lake)}$), and non-fossiliferous micrite (micrite facies, $M_{(lake)}$) are preserved in Stage 3. After either a depositional hiatus or erosion representing ~10 Myr, Stage 4 suggests a likely reinitiation of deformation in the region, represented by deposition of the final capping pebble to cobble conglomerate (Fetrow et al., 2020).

### 2.3. Seasonal Biases of Terrestrial Carbonate Records

To use terrestrial carbonate archives for paleoclimate interpretations, it is important to account for when in the year carbonates form, and therefore, identify to which season(s) their paleotemperature records correspond. The timing and extent of carbonate formation across depositional settings is the product of a combination of environmental factors that can include temperature, timing and style of precipitation, substrate texture and pH, presence or absence of vegetation, and concentration of major cation (e.g., $Ca^{2+}$, $Mg^{2+}$) and carbonate anions (i.e., $HCO_3^-$ and $CO_3^{2-}$; e.g., Breecker et al., 2009; Burgener et al., 2018; Huntington et al., 2010; Ingalls et al., 2020; Zamanian et al., 2016). While not much is known about palustrine carbonate formation, we can use lakes and soil carbonates as guides because palustrine environments exist on a gradient between these two environments. There is growing body of evidence that suggests that formation of soil carbonate nodules is principally controlled by increased carbonate saturation state due to enhanced transport of $Ca^{2+}$ from the surface into the soil column and evaporative concentration of $Ca^{2+}$ and $CO_3^{2-}$ ions in soil water that occurs during dry-down periods (Breecker et al., 2009; Burgener et al., 2016, 2018; Gallagher & Sheldon, 2016). These periods of significant wetting and drying cycles often correspond to warm seasons where precipitation cycles are more episodic and wetting and drying cycles can be more pronounced (Breecker et al., 2009; Hough et al., 2014; Kelson et al., 2020). Therefore, since pedogenic carbonate formation is found to preferentially occur during warm, episodically dry periods, clumped isotope temperatures may often reflect mean warmest month temperature rather than MAT (Breecker et al., 2009; Passey et al., 2010; Quade et al., 2013). Similarly, lacustrine carbonates typically preserve warm season bias, although the timing of precipitation in lacustrine settings is also controlled by seasonal mixing, alkalinity, influence of biologic activity, and evaporation (e.g., Huntington et al., 2010; Ingalls et al., 2020). Lacustrine carbonates may preserve cooler temperatures with commonly dampened expression of seasonal variability than palustrine carbonates due to a slower seasonal response of water temperature with increased water depth (Dee et al., 2021). Based on these findings, we expect a similar warm season bias in the formation of carbonate in palustrine environments in the NCF, but this remains an unresolved question since no studies have yet explored $\Delta_{47}$ thermometry in palustrine carbonate facies and few have explored $\delta^{13}C_{carb}$ and $\delta^{18}O_{carb}$ systematics.

## 3. Materials and Methods

### 3.1. Field and Hand Sample Preparation

We measured and described the stratigraphy of the NCF type section located east of Eureka, Nevada during field sessions in 2016 and 2017 (Figure 1). The field methods and resulting sedimentary interpretation from these field sessions were described in Fetrow et al. (2020). Hand samples ($n$ = 208) were collected from all exposed carbonate beds and the presence of carbonate in the samples was assessed in the field by testing for reactivity with dilute hydrochloric acid. We sampled carbonate beds at ~0.5 m increments throughout the vertical measured sections where exposure permitted or where we could dig to reasonable exposure, although due to thick overlying colluvium this was not possible in several intervals.

In addition to sampling up section through stratigraphic height, four "lateral transects" were measured and described, and samples were collected along-strike at four stratigraphic heights (21.5, 30, 317, 323 m; Figure 2). Two lateral sections were measured in the lower part of the type section (member Knc1; Stage 1) to document the lateral heterogeneity of the palustrine depositional landscape at two stratigraphic levels. The two lower NCF

lateral transects were approximately 20 m with hand samples collected taken every ~5 m. Two lateral sections were also measured in the upper part of the type section (member Knc4; Stage 3) to explore lateral heterogeneity and estimate lateral extent of the paleo-lake at two stratigraphic levels. The two upper NCF lateral transects were approximately 100 m with measurements taken every ~15 m when exposure allowed.

Hand samples were cut into billets and polished to expose unweathered faces that were used for making thin sections for petrographic analyses and drilling sample powder. Thin sections ($n$ = 69) were made by Spectrum Petrographics, Inc. Samples from which $\delta^{13}C$, $\delta^{18}O_{carb}$, and $\Delta_{47}$ isotope analyses were measured were assessed for diagenetic changes using optical and cathodoluminescence petrography (see section below, and Fetrow et al., 2020). Carbonate mineralogy was determined by petrographic inspection, and, for a subset of samples, XRD analysis. XRD analyses were conducted on 21 NCF samples on a Bruker D8 Advance that uses Cu K-alpha radiation and the spectra were processed using Bruker *Diffrac.eva* software to match unknown spectra to the International Center for Diffraction Data (ICDD) database of known spectra. Representative samples of each of the different carbonate-bearing facies were the primary targets selected for XRD analysis (Table S1).

To prepare samples for geochemical analyses, a dental drill was used to generate ~30–50 mg of fine powder from each hand sample and then homogenized using a mortar and pestle. All isotope analyses were generated from subsamples of this homogenized powder. If additional sample powder was drilled from a sample, we compared the isotopic values and temperature estimates of the two generations of sample powder and considered them "one sample" only if the values of the two generations fell within 1 standard error (1 s.e.) of one another for all measured isotopes. Where quantities allowed, additional spots were drilled from some hand samples to target secondary spars or regions of variable textures, such as microsparite or sparite, to determine isotopic values and formation temperatures of diagenetic events or fluids that created the secondary spars. Some hand samples were subsampled to explore cm-scale heterogeneity, such as regions of lighter and darker colored micrite, in palustrine and lacustrine carbonate-bearing facies (e.g., sample *AF-NCF-TS2-17-21.5A*). More detailed facies descriptions for the lateral sections measured in the NCF type section can be found in Figure 2 in Fetrow et al. (2020) and in the Supporting Information (Figures S4 and S5 in Supporting Information S1).

Crystalline spar veins were sub-sampled from two NCF carbonate samples from the lower palustrine unit (Stage 1) at stratigraphic heights of 21.5 and 75.6 m (*21.5D_spar* and *31_spar*) (Figure 2). *21.5D_spar* occurs in a pebbly pelmicrite sample and *31_spar* occurs in a mottled micrite sample. Spar veins were sampled carefully using a dissecting microscope to avoid inclusion of the surrounding matrix. In addition, a hand sample of the underlying Carboniferous Ely Limestone was collected just east of the exposure of the NCF type section along the Newark Canyon Road. The sample of Ely Limestone ("Ely LS") and a spar vein found within the sample ("Ely Spar") were analyzed as isotopic reference points to be compared against NCF samples.

### 3.2. Optical and Cathodoluminescence Microscopy

We used optical and cathodoluminescence microscopy to identify primary depositional fabrics, as well as diagenetic fabrics that may have resulted from dissolution and/or reprecipitation, recrystallization, and later void-filling cements in samples used for $\delta^{13}C_{carb}$, $\delta^{18}O_{carb}$, and $\Delta_{47}$ analyses. Optical and cathodoluminescence (CL) images are shown for representative samples chosen from carbonate facies (Figures S1–S3 in Supporting Information S1). Samples with >3 clumped isotope replicates and low standard error for bulk $\delta^{13}C$ and $\delta^{18}O_{carb}$ (<0.02‰ and <0.03‰, respectively) were used as representative examples of the carbonate-bearing facies for the petrographic image plates. CL microscopy was conducted on a Technosyn Cathode Luminescence Model 8200 Mk II microscope. CL colors from carbonate minerals vary between yellow, orange, and red to dull to non-luminescent according to the spatial distribution of trace elements (i.e., Fe and Mn) in carbonate fabrics and the mineralogy (Pagel et al., 2000). CL imaging can be used as a visual aid in determining generations of crystallization through crosscutting relationships and to yield useful information about primary and diagenetic components of carbonate facies (Dunagan & Driese, 1999; Mintz et al., 2011; Wright & Peeters, 1989).

### 3.3. Stable Single Carbon and Oxygen Isotopes ($\delta^{13}C$ and $\delta^{18}O_{carb}$) Analytical Procedure

Approximately 110–250 µg of sample powder (equivalent to ~100–110 µg of pure carbonate mineral) was weighed into Labco Exetainers vials (12 ml) and purged with ultra-high purity He for 5 min. Samples were digested in 105%–110% orthophosphoric acid at 70°C for >30 min to release $CO_2$ for analysis. A linear regression between

the known sample mass and the intensity on the mass 44 detector was used to calculate the weight percent carbonate (i.e., "wt% carbonate") for each sample. Samples ($n = 181$) were analyzed for $\delta^{13}C$ and $\delta^{18}O_{carb}$ using a Thermo Scientific GasBench II coupled to a Thermo Delta V continuous flow isotope ratio mass spectrometer in the CU Boulder Earth Systems Stable Isotope Laboratory (CUBES-SIL; RRID SCR-019300). All stable isotope ratios are reported in delta ($\delta$) notation as the per mil (‰) deviation relative to the Vienna Pee Dee Belemnite (VPDB) standard, where $\delta = ([(R_{Sample}/R_{Standard}) - 1] \times 1{,}000)$, and $R$ is the ratio of the heavier mass isotope to the lighter mass isotope. Repeated measurements of in-house and internationally accepted carbonate standards (i.e., Icelandic Spar (HIS), NBS19, and CU YULE, an in-house marble standard) yielded precision of ±0.1 ‰ or better for both $\delta^{13}C$ and $\delta^{18}O_{carb}$. To correct raw values, the *Isoreader R* package was used to read all raw data files directly into *R* (Kopf et al., 2021). Values were evaluated for and then corrected for the effects of linearity and drift, if identified. These corrected values, rather than the raw values, were then used in a scale correction. Linearity, drift, and scale corrections to data were done using in-house CUBES-SIL *R* scripts that utilized *tidyverse* (v. 1.3.1) and *isoprocessor* (v. 0.6.5) packages. There was a consistent average offset of 0.7‰ and 0.14‰ for bulk $\delta^{13}C_{carb}$ and $\delta^{18}O_{carb}$ values, respectively, for data generated on both the Delta V and 253 Plus. We accounted for this by calculating a sample mean and standard error weighted by the standard error for each analyzed aliquot of sample powder analyzed on the two machines. Errors for $\delta^{13}C$ and $\delta^{18}O_{carb}$ measurements reported in the text and in all figures represent two standard error (i.e., 2 s.e.) of the mean (Table S2).

### 3.4. Clumped Isotopes ($\Delta_{47}$) Analytical Procedure

As temperature decreases, it is thermodynamically favorable to form more doubly substituted carbonate isotopologues that include both the heavy isotopes of carbon and oxygen ($^{13}C^{18}O^{16}O^{2-}$, termed "clumps"; Eiler, 2007, 2011); this inverse relationship between temperature and "clumping" is used as a paleothermometer (Anderson et al., 2021; Ghosh et al., 2006). Clumped isotope analyses were performed on 58 samples that appeared well preserved based on petrographic inspection, as well as on some samples with identifiable diagenetic fabrics and secondary spar inclusions (Table S3). Calcium carbonate standards (e.g., ETH1–4, IAEA-C1 and C2, Merck, and NBS19) were analyzed at a standard-to-sample ratio of ~1:1 and were used to correct the data to the community accepted Intercarb-Carbon Dioxide Equilibrium Scale (ICDES; Bernasconi et al., 2021). Only three standards are needed for the correction, and additional standards were used to assess the effectiveness of the data corrections. In addition to carbonate standards, gases equilibrated to 25°C ("equilibrated") and 1,000°C ("heated") that spanned a large range of $\delta^{47}$ values were measured to provide an extended reference frame for samples with very high or low $\delta^{47}$ values; because all the sample data were within the bounds of the carbonate standards, the gases were not used to correct the samples to the ICDES reference frame.

For samples and carbonate standards, approximately 6–12 mg of carbonate powder was weighed into silver capsules for each analysis. The powders were digested in 90°C phosphoric acid for 45 min and the evolved $CO_2$ was analyzed for the abundance of masses 44–49 of $CO_2$, and use to determine $\Delta_{47}$, $\delta^{47}$, $\delta^{13}C_{carb}$, and $\delta^{18}O_{carb}$ values for each sample. Values are reported as $\Delta_{47}$ (‰, ICDES) which is defined as the deviation in the measured ratio of doubly substituted mass-47 $CO_2$ ($^{13}C^{18}O^{16}O$) isotopologues to the more abundant mass-44 ($^{12}C^{16}O_2$) isotopologue, $R^{47}_{sample} = M^{47}_{sample}/M^{44}_{sample}$ compared to the expected $R^{47}$ for a stochastic distribution of isotopes (Schauble et al., 2006):

$$\Delta_{47}(‰) = \left(\frac{R^{47}_{sample}}{R^{47}_{stochastic}} - 1\right) * 1{,}000 \quad (1)$$

$\Delta_{47}$ data were collected across five sessions between 2019 and 2022 on a Thermo Scientific 253 Plus dual-inlet isotope ratio mass spectrometer in the CUBES–SIL (Table S4). Details about the analytical setup and each run session (AF8–AF12), including the number of acquisitions, reference gas/sample gas cycles per acquisition, standard gases and carbonates measured, can be found in the Supporting Information. Precision of individual analyses is reported as two standard errors of the mean (2 s.e.) and includes analytical error of each measurement as well as errors associated with the correction lines used (Bernasconi et al., 2021; Dennis et al., 2011; Huntington et al., 2009). All $\Delta_{47}$ values for samples reported here, and used to calculate temperatures, are based on averages of 3–9 replicates that were typically analyzed across different sessions (Table S3). Outlier replicates for each sample were culled if they were outside of the two standard deviations of the replicate mean in any isotope. $\Delta_{47}$ values were calculated as weighted means of all the replicates, and associated errors were calculated using

10.1029/2022PA004517

**Table 2**
*Facies Averages Including All Samples*

| Facies | Samples per facies for $\delta^{18}O_{carb}$ | Median $\delta^{13}C$ (‰, VDPB) | Mean $\delta^{13}C$ (‰, VDPB) | $\delta^{13}C$ 2 s.e. | $\delta^{13}C$ maximum | $\delta^{13}C$ minimum | Median $\delta^{18}O_{carb}$ (‰, VDPB) | Mean $\delta^{18}O_{carb}$ (‰, VDPB) | $\delta^{18}O_{carb}$ 2 s.e. | $\delta^{18}O_{carb}$ maximum | $\delta^{18}O_{carb}$ minimum | Samples per facies for $T(\Delta_{47})$ and $\delta^{18}O_{water}$ | Median $\delta^{18}O_{water}$ (‰, VDPB) | Mean $\delta^{18}O_{water}$ (‰, VDPB) | $\delta^{18}O_{water}$ 2s.e. | $\delta^{18}O_{water}$ maximum | $\delta^{18}O_{water}$ minimum | Median $T(\Delta_{47})$ (°C) | Mean $T(\Delta_{47})$ (°C) | $T(\Delta_{47})$ 2 s.e. | $T(\Delta_{47})$ maximum | $T(\Delta_{47})$ minimum |
|---|---|---|---|---|---|---|---|---|---|---|---|---|---|---|---|---|---|---|---|---|---|---|
| Ely | 1 | 2.26 | 2.26 | 0.04 | 2.26 | 2.26 | −6.18 | −6.18 | 0.31 | −6.18 | −6.18 | 1 | 7.90 | 7.90 | 2.20 | 7.90 | 7.90 | 96.0 | 96.0 | 15.8 | 96.0 | 96.0 |
| Ely Spar | 2 | −0.47 | −0.47 | 0.20 | −0.36 | −0.57 | −16.99 | −16.99 | 1.04 | −16.47 | −17.51 | 2 | −0.35 | −0.35 | 1.90 | 0.60 | −1.30 | 117.9 | 117.9 | 7.2 | 121.5 | 114.3 |
| $Fc_{lake}$ | 7 | −0.25 | −1.03 | 2.07 | 1.05 | −6.69 | −9.40 | −9.40 | 1.16 | −6.35 | −10.64 | 1 | −2.30 | −2.30 | 1.20 | −2.30 | −2.30 | 57.8 | 57.8 | 7.0 | 57.8 | 57.8 |
| $Gc_{channel}$ | 1 | −3.68 | −3.68 | 0.06 | −3.68 | −3.68 | −8.25 | −8.25 | 0.33 | −8.25 | −8.25 | 1 | −2.30 | −2.30 | 2.60 | −2.30 | −2.30 | 43.7 | 43.7 | 14.6 | 43.7 | 43.7 |
| $M_{lake}$ | 30 | −3.71 | −3.39 | 0.44 | 1.29 | −5.25 | −3.58 | −3.58 | 0.80 | −1.37 | −10.13 | 18 | 1.95 | 1.95 | 0.80 | 5.00 | −3.50 | 40.2 | 40.3 | 2.4 | 55.1 | 29.1 |
| $Mb_{lake}$ | 19 | −1.68 | −1.55 | 1.21 | 2.15 | −7.05 | −8.07 | −8.07 | 1.33 | −3.56 | −13.80 | 11 | −0.44 | −0.44 | 1.42 | 3.70 | −7.80 | 48.3 | 50.7 | 4.4 | 68.4 | 40.1 |
| $Mb_{pond}$ | 12 | −4.67 | −4.79 | 0.56 | −3.30 | −6.24 | −9.62 | −9.62 | 0.74 | −7.35 | −11.94 | 3 | −3.20 | −3.20 | 0.81 | −1.70 | −4.50 | 43.1 | 49.9 | 8.5 | 66.7 | 39.9 |
| $Mm_{wetland}$ | 17 | −4.33 | −4.45 | 0.36 | −3.41 | −6.23 | −8.12 | −8.12 | 0.81 | −4.67 | −10.96 | 7 | −0.30 | −0.30 | 0.44 | 0.70 | −1.30 | 53.6 | 52.0 | 5.2 | 68.4 | 36.4 |
| $Mn_{soil}$ | 4 | −5.67 | −5.42 | 1.37 | −3.56 | −6.80 | −8.94 | −8.94 | 0.73 | −8.14 | −9.86 | 1 | −3.70 | −3.70 | 1.60 | −3.70 | −3.70 | 45.0 | 45.0 | 9.0 | 45.0 | 45.0 |
| $Mp_{wetland}$ | 32 | −4.32 | −4.32 | 0.29 | −3.07 | −6.23 | −8.96 | −8.96 | 0.46 | −5.78 | −11.35 | 15 | −2.07 | −2.07 | 0.57 | 1.20 | −4.40 | 44.8 | 46.8 | 3.6 | 66.5 | 28.3 |
| Spar | 2 | −4.34 | −4.34 | 3.47 | −2.61 | −6.08 | −11.94 | −11.94 | 5.17 | −9.36 | −14.53 | 2 | 2.30 | 2.30 | 13.00 | 8.80 | −4.20 | 100.3 | 100.3 | 59.8 | 130.2 | 70.4 |

standard errors of the replicates as the weighting factors, following Huntington et al. (2009). The median of the replicates for each sample was also calculated as a comparison to the weighted mean values for $\delta^{18}O_{water}$ and $T(\Delta_{47})$ estimates. Mean $\Delta_{47}$ precision of carbonate standards across all run sessions is 0.012‰ ($\pm 2.8 \times 10^{-4}$, 2 s.e.). Temperatures were estimated from the mean $\Delta_{47}$ values using the Anderson et al. (2021) calibration line, and temperature uncertainties were estimated by taking into account the $\Delta_{47}$ standard error for every sample; all plots show two standard errors (2 s.e.) for $T(\Delta_{47})$. From the measured $\Delta_{47}$ temperature and $\delta^{18}O_{carb}$ values, the $\delta^{18}O$ of the water ($\delta^{18}O_{water}$) in which the carbonate sample precipitated was calculated using the equilibrium fractionation between calcite and water established by Kim and O'Neil (1997). $\delta^{18}O_{water}$ is reported relative to the VSMOW reference frame (Coplen, 2011). Errors for $\delta^{18}O_{water}$ measurements reported in the text and in all figures represent 2 s.e. of the mean and incorporate the error from $\Delta_{47}$ measurements.

## 4. Results

There is significant variability in $\delta^{13}C$, $\delta^{18}O_{carb}$, $\delta^{18}O_{water}$, and $T(\Delta_{47})$ estimates across all NCF facies analyzed (Table 2). $\delta^{13}C$ values range from approximately −7.05‰ to +2.26‰ and $\delta^{18}O_{carb}$ values range from approximately −13.80‰ to −1.37‰. $\delta^{18}O_{water}$ values range from approximately −7.80‰ to +5.00‰ and $T(\Delta_{47})$ estimates span from ∼28 to 68°C.

### 4.1. Palustrine Facies—Lower NCF (∼113–112 Ma)

For the palustrine facies, the mean $\delta^{13}C$ value for $Mp_{(wetland)}$ and $Mm_{(wetland)}$ are similar, −4.32‰ (±0.29‰, 2 s.e.) and −4.45‰ (±0.36‰, 2 s.e.), respectively (Table 2). The one $Gc_{(channel)}$ sample analyzed has a $\delta^{13}C$ value of −3.68‰ (±0.06‰, 2 s.e.). The $Mb_{(pond)}$ and associated $Mn_{(soil)}$ facies have the most negative $\delta^{13}C$ values with average $\delta^{13}C$ values of −4.79‰ (±0.56‰, 2 s.e.) and −5.42‰ (±1.37‰, 2 s.e.), respectively.

The $Mm_{(wetland)}$ facies has the most positive $\delta^{18}O_{carb}$ values among the four palustrine facies. The $Mm_{(wetland)}$ facies has an average $\delta^{18}O_{carb}$ value of −8.12‰ (±0.81‰, 2 s.e.) and ranges from −10.96‰ to −4.67‰. The $\delta^{18}O_{carb}$ values for the $Mp_{(wetland)}$ facies range from approximately −11.35‰ to −5.78‰ with an average $\delta^{18}O_{carb}$ of −8.96‰ (±0.46‰, 2 s.e.). The $Mb_{(pond)}$ and $Mn_{(soil)}$ facies have average $\delta^{18}O_{carb}$ values of −9.62‰ (±0.74‰, 2 s.e.) and −8.94 ‰ (±0.73‰, 2 s.e.), respectively. The calcareous conglomerate ($Gc_{(channel)}$) sample analyzed has a $\delta^{18}O_{carb}$ value of −8.25‰ (±0.33‰, 2 s.e.).

The $Mm_{(wetland)}$ facies has higher $\delta^{18}O_{water}$ values than the $Mp_{(wetland)}$ facies by approximately 2‰. The $Mm_{(wetland)}$ facies has an average $\delta^{18}O_{water}$ value of −0.30‰ (±0.44‰, 2 s.e.) and the $Mp_{(wetland)}$ facies has an average of −2.07‰ (±0.57‰, 2 s.e.). The $Mb_{(pond)}$ and one sample from the $Mn_{(soil)}$ facies have a $\delta^{18}O_{water}$ values of −3.20‰ (±0.81‰, 2 s.e.) and −3.70‰ (±1.60‰, 2 s.e.), respectively. The $Gc_{(channel)}$ sample analyzed has a $\delta^{18}O_{carb}$ value of −2.30‰ (±2.6‰, 2 s.e.).

The $Mp_{(wetland)}$ facies has a mean $T(\Delta_{47})$ of 46.8°C (±3.6°C, 2 s.e., $n = 15$) and the $Mm_{(wetland)}$ facies has a hotter mean $T(\Delta_{47})$ of 52.0°C (±5.2°C, 2 s.e., $n = 7$). The one $Gc_{(channel)}$ sample analyzed has a $T(\Delta_{47})$ estimate of 43.7°C (±14.6°C, 2 s.e.). Fewer samples of the $Mb_{(pond)}$ ($n = 3$) and $Mn_{(soil)}$ ($n = 1$) facies were fully replicated than the $Mp_{(wetland)}$ and $Mm_{(wetland)}$ facies. $Mb_{(pond)}$ and $Mn_{(soil)}$ have average $T(\Delta_{47})$ estimates, 49.9°C (±8.5°C, 2 s.e.) and 45.0°C (±9.0°C, 2 s.e.), respectively.

### 4.2. Lacustrine Facies—Upper NCF (~112–103 Ma)

Both the $Mb_{(lake)}$ and $M_{(lake)}$ have considerable variability in $\delta^{13}C$ values compared to the palustrine facies. The $M_{(lake)}$ has an average $\delta^{13}C$ of −3.39‰ (±0.44‰, 2 s.e.) and the $Mb_{(lake)}$ has an average of −1.55‰ (±1.21‰, 2 s.e.). $\delta^{13}C$ values from the $Mb_{(lake)}$ facies spans from −7.05‰ to +2.15‰ and the $M_{(lake)}$ facies spans from −5.25‰ to +1.29‰. The $Fc_{(lake)}$ facies has an average $\delta^{13}C$ of −1.03‰ (±2.07‰, 2 s.e.) and ranges notably from −6.69‰ to +1.05‰.

The $M_{(lake)}$ facies, which is the dominant facies preserved in the upper lacustrine section, has an average $\delta^{18}O_{carb}$ value of −3.58‰ (±0.80‰, 2 s.e.) and has consistently higher $\delta^{18}O_{carb}$ values than the palustrine facies. The $\delta^{18}O_{carb}$ values for the $Mb_{(lake)}$ facies, which is the main facies in the lower lacustrine section, range from approximately −13.80‰ to −3.56‰ with an average of −8.07‰ (±1.33‰, 2 s.e.). The spread in $\delta^{18}O_{carb}$ for the $Mb_{(lake)}$ facies is larger than the variability across the $M_{(lake)}$ facies and all the palustrine facies combined.

The $\delta^{18}O_{water}$ values for the $M_{(lake)}$ facies in the upper lacustrine section averages +1.95‰ (±0.80‰, 2 s.e.) and is consistently higher than the palustrine facies. The samples from the lower lacustrine section, dominated by the $Mb_{(lake)}$ facies, are lower than the upper lacustrine samples (−0.44‰(±1.42‰, 2 s.e.)) and have a broad spread in $\delta^{18}O_{water}$ values (−7.80‰. to +3.70‰). The $M_{(lake)}$ facies has a mean $T(\Delta_{47})$ of 40.3°C (±2.4°C, 2 s.e., $n = 18$), while the $Mb_{(lake)}$ facies has a mean $T(\Delta_{47})$ ~10°C hotter, at 50.7°C (±4.4°C, 2 s.e., $n = 11$). The one $Fc_{(lake)}$ facies analyzed for $T(\Delta_{47})$ has a temperature estimate of 57.8°C (±7.0°C, 2 s.e., $n = 1$).

### 4.3. Secondary Spar

The NCF secondary spars (*31_spar* and *21.5D_spar*) have $\delta^{13}C$ values of −2.61‰ (±0.19‰, 2 s.e.) and −6.08‰ (±0.001‰, 2 s.e.), respectively, while the secondary spar from the Ely Limestone has an average $\delta^{13}C$ value of −0.47‰ (±0.20‰, 2 s.e.). The Ely Limestone has a $\delta^{13}C$ value of +2.26‰ (±0.06‰, 2 s.e.). The NCF secondary spars (*31_spar* and *21.5D_spar*) have $\delta^{18}O_{carb}$ values of −9.36‰ (±0.14‰, 2 s.e.) and −14.53‰ (±0.004‰, 2 s.e.), respectively, while the secondary spar from the Ely Limestone has a $\delta^{18}O_{carb}$ value of −16.99‰ (±1.04, 2 s.e.). The Ely Limestone has a $\delta^{18}O_{carb}$ value of −6.29‰ (±0.28‰, 2 s.e.).

The NCF secondary spars (*31_spar* and *21.5D_spar*) have $\delta^{18}O_{water}$ values of +8.80‰ (±2.4‰, 2 s.e.) and −4.2‰ (±1.4‰, 2 s.e.), respectively, while the secondary spar from the Ely Limestone has a $\delta^{18}O_{water}$ value of −0.35‰ (±1.90‰, 2 s.e.). The Ely Limestone has a $\delta^{18}O_{water}$ value of +7.90‰ (±2.20‰, 2 s.e.). The Ely Limestone has an average $T(\Delta_{47})$ estimate of 96.0°C (±15.8°C, 2 s.e.). The Ely Limestone spar has an average $T(\Delta_{47})$ estimate of 117.9°C (±7.2°C, 2 s.e.) and the NCF spars (*31_spar* and *21.5D_spar*) have $T(\Delta_{47})$ estimate of 130.2°C (±22.2°C, 2 s.e.) and 70.4°C (±9.8°C, 2 s.e.), respectively.

## 5. Discussion

Before it is possible to use the carbon, oxygen, and clumped isotope records from the NCF to interpret the paleoclimate, paleoenvironment, and paleoelevation of the terrestrial western USA in the mid-Cretaceous, we must account for diagenetic changes to the isotopic record. The presence of cross-cutting spar veins, discrete spar crystals of calcite and dolomite, and sparite in the NCF demonstrate that the rocks experienced high temperatures, either from deep burial or interaction with hot fluids from depth, or both. In the following sections, we evaluate possible impacts of diagenesis associated with solid state reordering and/or from hydrothermal fluids, and disentangle these effects from the primary depositional mechanisms that drive isotopic variability (Figure 4).

### 5.1. Solid State Reordering

Laboratory heating experiments and numerical modeling of bond ordering have shown that $\Delta_{47}$ values of calcite samples will reorder via solid state diffusion if exposed to temperatures in excess of ~100°C for $10^6$–$10^8$ yr (Henkes et al., 2014; Passey & Henkes, 2012). This process is called solid-state reordering and can occur regardless of the bulk isotope composition of the mineral (i.e., $\delta^{47}$). In theory, if two carbonate-bearing rocks with different primary $T(\Delta_{47})$ values fully equilibrate to a new, hotter temperature by solid state reordering they will both record the same new $T(\Delta_{47})$ estimate. If solid state reordering had significantly impacted $T(\Delta_{47})$ values from the NCF, we would expect to see little variability in $T(\Delta_{47})$ and $\delta^{18}O_{water}$ values between carbonate facies at

similar stratigraphic heights. In particular, we would expect carbonate facies that are closely interbedded in the palustrine and lacustrine portions of the record, such as $Mp_{(wetland)}$ versus $Mm_{(wetland)}$ and $M_{(lake)}$ versus $Mb_{(lake)}$, to preserve similar $T(\Delta_{47})$ values. Instead, $T(\Delta_{47})$ estimates are distinctive between facies throughout the NCF record (Figures 5 and 6, and Figures S4 and S5 in Supporting Information S1).

The burial history the Cretaceous NCF and underlying formations also suggests limited impacts on $T(\Delta_{47})$ from solid state reordering. The NCF in the southern Diamond Mountains overlies the Permian Carbon Ridge Formation across an unconformity, and is locally projected to overlie the Carboniferous Ely Limestone (Di Fiori et al., 2020; Long, Henry, Muntean, Edmondo, & Cassel, 2014; Long, Henry, Muntean, Edmondo, & Thomas, 2014; Nolan et al., 1956). This demonstrates that the Paleozoic section in this region was buried at least two times: first during deposition of the Paleozoic sedimentary sequence ("burial 1"), and then a second time after exhumation to the surface and burial during deposition of the NCF and possible other overlying younger sediments ("burial 2"). Peak temperature estimates for the Ely Limestone in the Grant Range, ~160 km southeast of the NCF type section, of 99 and 144°C were found using Rock-Eval pyrolysis and vitrinite reflectance, respectively (Long & Soignard, 2016). Using the hotter vitrinite reflectance temperature for the Ely Limestone (144°C) and assuming the average geothermal gradient of ~50°C/km for this region of the Sevier hinterland during the Cretaceous (e.g., Long & Soignard, 2016; Zuza et al., 2020), the Ely Limestone experienced an approximate burial depth of ~3 km. If the peak temperature estimates reflect "burial 1" of the Carbon Ridge and Ely Limestone, then this implies that the maximum burial of the NCF is not much more than its thickness of ~500 m (Di Fiori et al., 2020; Fetrow et al., 2020; Long, Henry, Muntean, Edmondo, & Cassel, 2014; Long, Henry, Muntean, Edmondo, & Thomas, 2014). There is very little indication that a thick sequence of younger sedimentary rocks was deposited on top of the NCF. However, this cannot be discounted and therefore we must consider whether these peak temperatures were reached during "burial 2" of the Carbon Ridge and the Ely Limestone. If so, the combined thickness of ~1 km for the Carbon Ridge Fm. and Ely Limestone plus the ~500 m thickness of the NCF means that the NCF could not have been buried under more than ~1.5 km of younger sediments. Using 1.5 km as

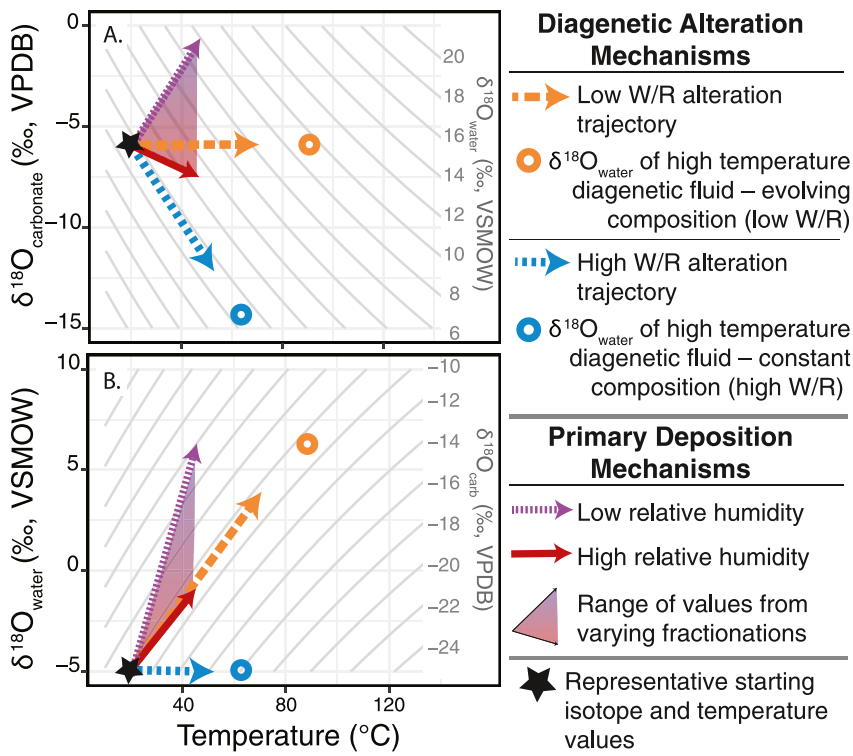


**Figure 4.** Schematic of $\delta^{18}O_{carb}$ (‰, VPDB) and $\delta^{18}O_{water}$ (‰, VSMOW) plotted against $T(\Delta_{47})$ estimates (°C) with trajectories illustrating the range of values expected from processes of low and high *W/R* ratio alteration and evaporative enrichment that could occur on the primary depositional landscape. Fluid composition values are illustrative. Contour lines in each plot represent corresponding $\delta^{18}O_{carb}$ (‰, VPDB) or $\delta^{18}O_{water}$ (‰, VSMOW) values, respectively. Framework modified from Bergmann et al. (2018).

the maximum burial depth for the NCF and assuming the same regional average geothermal gradient of ~50°C/km, the maximum burial temperatures for the NCF did not exceed ~75°C in this "burial 2" scenario. Based on burial of the NCF to 0.5–1.5 km, it is unlikely that the entirety of the NCF type section experienced temperatures >100°C long enough to generate solid-state reordering. Given the lack of necessary burial, other mechanisms, such as more localized secondary alteration and/or extreme primary depositional conditions, must be responsible for the range of temperatures and isotope values.

### 5.2. Disentangling Hydrothermal Diagenesis From Primary Depositional Processes

#### 5.2.1. Framework for Evaluating Hydrothermal Alteration

Plots of $\delta^{18}O_{carb}$ and $\delta^{18}O_{water}$ against $T(\Delta_{47})$ estimates provide a framework of endmember isotope and temperature scenarios that can be used to identify diagenetic effects on the NCF stable isotope values (Bergmann et al., 2018; Goldberg et al., 2021; Ryb et al., 2021; Figure 4).

*Diagenetic Scenario 1* (Figure 4, blue line): During diagenetic alteration via fluids with a high water to rock (*W*/*R*) ratio, as the temperature of the system steadily increases, the $\delta^{18}O_{carb}$ value will evolve along the contour of constant $\delta^{18}O_{water}$ (Figure 4a, diagonal blue line). This assumes that diagenesis occurs in an open system with abundant fluids, which allows the diagenetic fluid to maintain a constant $\delta^{18}O_{water}$ value (Figure 4b, horizontal blue line). Complete isotopic exchange with the diagenetic fluid will create $\delta^{18}O_{carb}$ of the rock that matches the $\delta^{18}O_{carb}$ of secondary carbonate that precipitates directly from the fluid (Figure 4a, blue dot and line).

*Diagenetic Scenario 2* (Figure 4, orange line): Under conditions with a very low *W*/*R* ratio, $\delta^{18}O_{carb}$ of the rock remains constant (Figure 4a, orange line) as temperature increases (i.e., "rock-buffered" isotopic exchange), while $\delta^{18}O_{water}$ values evolve (Figure 4b, orange line). Solid state reordering, as previously discussed, can be considered an extreme version of this endmember, but in that case, the evolving $\delta^{18}O_{water}$ values are not a true reflection of the $\delta^{18}O_{water}$ of fluids, because no fluids are involved in solid state reordering.

#### 5.2.2. Framework for Evaluating Primary Depositional Mechanisms

When considering the possible effects of alteration, it is important to also consider how isotopes and temperature will reflect various environmental changes across the primary depositional landscape, as some processes may result in isotopic trends that are similar to alteration trajectories. For example, the wetlands that deposited the $Mp_{(wetland)}$ and $Mm_{(wetland)}$ likely experienced variations in the amount of evaporation or radiative heating of the water and ground, which would have propagated to the $\delta^{18}O_{carb}$, $\delta^{18}O_{water}$, and $T(\Delta_{47})$ values of these facies. The purple dashed and red solid lines in Figure 4 represent theoretical trajectories in which temperature increases under high and low relative humidity conditions. The degree of fractionation between liquid and vapor ($\alpha_{water\text{-}vapor}$) decreases with increasing relative humidity, enabled by increased exchange between the liquid and vapor as the system approaches equilibrium exchange (Chacko et al., 2019; Gonfiantini et al., 2018). Conversely, there is more fractionation between liquid and vapor (higher $\alpha_{water\text{-}vapor}$) at lower relative humidity conditions, and therefore, the residual liquid water becomes more enriched in $^{18}O$ (Dansgaard, 1964; Luz et al., 2009).

Applying this to the NCF, higher $\alpha_{water\text{-}vapor}$ resulting from low relative humidity conditions would generate a residual water body, such as a wetland, that is more evaporatively $^{18}O$-enriched. Any subsequent carbonate minerals that precipitated from the $^{18}O$-enriched water would have higher $\delta^{18}O_{carb}$ values. The shaded region between the theoretical high and low fractionation trajectories represents a gradient of possible isotope compositions that could occur depending on the relative humidity and resulting $\alpha_{water\text{-}vapor}$. Evaporative enrichment must be considered given the sedimentological evidence that evaporation was a key driver of depositional heterogeneity in the palustrine environments of the lower NCF type section, such as the presence of mud cracking and pseudo-microkarsting (Fetrow et al., 2020). Notably, the low fractionation scenario (red line) results in evolution of $\delta^{18}O_{carb}$, $\delta^{18}O_{water}$, and $T(\Delta_{47})$ values that are similar to the trajectories of diagenetic alteration under low *W*/*R* conditions, although the upper temperature limit for evaporation in a surface environment is likely lower than for low *W*/*R* alteration. These two evaporation scenarios are simplified for illustrative purposes, and exclude the consideration of other environmental conditions that influence evaporation, such as wind speed, water body surface area, and salinity (Harbeck, 1962).

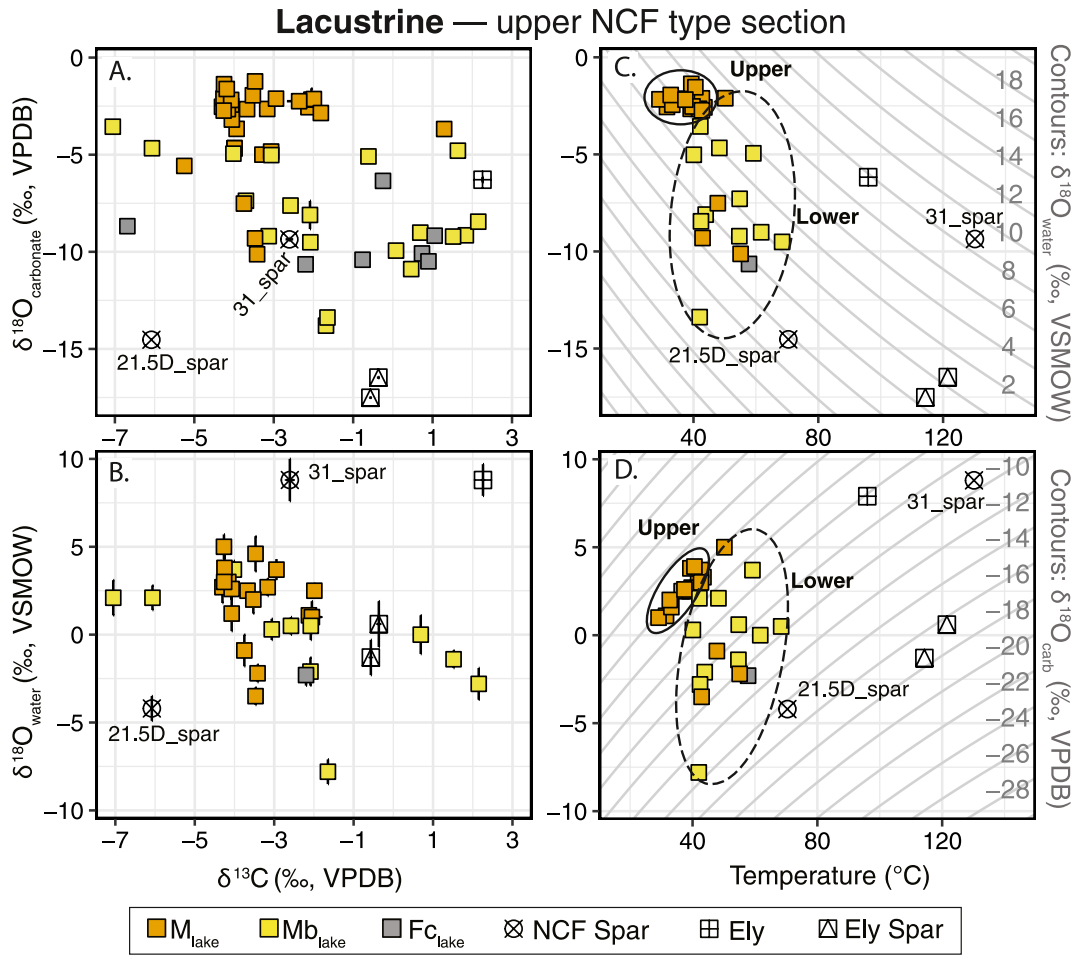


**Figure 5.** Bivariate plots for lacustrine samples from Stage 3 of the Newark Canyon Formation (NCF) type section. Solid and dashed circles denote lacustrine samples from the upper and lower portion of Stage 3, respectively. Symbols colored by facies. (a) $\delta^{13}C$ (‰, VPDB) versus $\delta^{18}O_{carb}$ (‰, VPDB). (b) $\delta^{13}C$ (‰, VPDB) versus $\delta^{18}O_{water}$ (‰, VSMOW). Error bars plotted for subplots A and B represent two standard error (2 s.e.) about the sample mean and unless visible, error bars are smaller than the datapoint. (c) $T(\Delta_{47})$ estimates versus $\delta^{18}O_{carb}$ (‰, VPDB). (d) $T(\Delta_{47})$ estimates versus $\delta^{18}O_{water}$ (‰, VSMOW). Error bars were omitted from subplots (c and d) for visual clarity and are reported in Figure 8 and Table S2.

### 5.3. Assessing Diagenesis Versus Depositional Signals

The lower palustrine and upper lacustrine units in the NCF type section are separated by likely >5 Myr of deposition and/or sedimentary hiatuses (Figure 2), and therefore, the stratigraphic order may not directly dictate the alteration history of each unit. Accounting for this stratigraphic separation, we will first consider lacustrine data separately from the palustrine data (Figures 5 and 6).

#### 5.3.1. Upper NCF (~112–103 Ma)—Lacustrine Facies

The top of the NCF type section records lacustrine sedimentation in which two interbedded, carbonate-bearing subfacies were deposited, the biomicrite ($Mb_{(lake)}$) and the massive micrite ($M_{(lake)}$). The lower half of the lacustrine samples, which are mostly the $Mb_{(lake)}$ facies, exhibit a wide range in $\delta^{13}C$ and $\delta^{18}O_{carb}$ values and have isotopic compositions closest to the Ely Limestone and secondary spars from the Ely and NCF samples (Figures 5a and 5c). This group of lacustrine samples are all from the stratigraphically lower portion of the lake unit (~300–321 m). The lower lacustrine samples have consistently higher $T(\Delta_{47})$ estimates and more negative $\delta^{18}O_{water}$ and $\delta^{18}O_{carb}$ values than upper lacustrine samples, regardless of facies type. We observe some spread of the lower lacustrine data along $\delta^{18}O_{water}$ contours (like Scenario 1, blue line) toward the *21.5D_spar* (Figure 5a). The scattering of

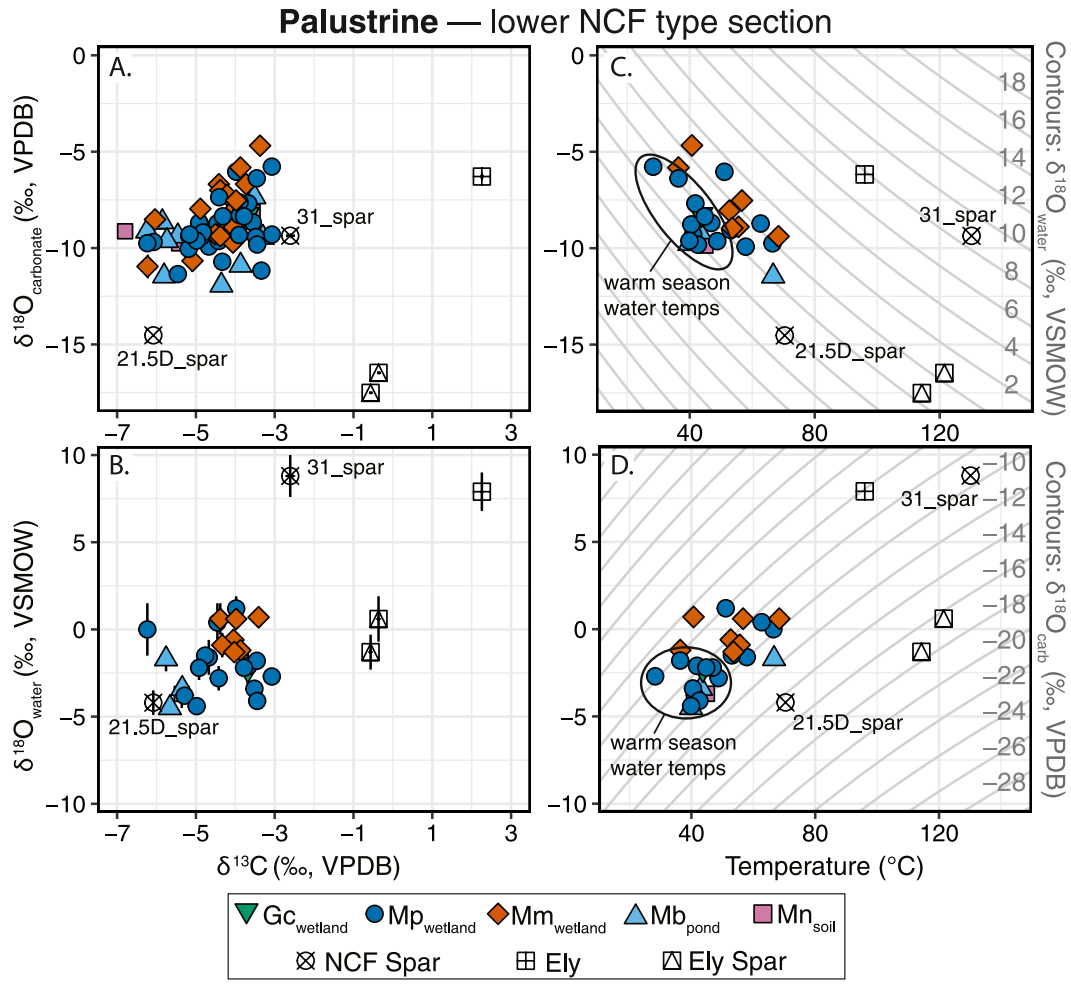


**Figure 6.** Bivariate plots for palustrine samples from Stage 1 of the Newark Canyon Formation (NCF) type section. Solid circle denotes palustrine samples estimated to preserve $T(\Delta_{47})$ values representative of primary warm season water temperatures. Symbols shaped and colored by facies. (a) $\delta^{13}C$ (‰, VPDB) versus $\delta^{18}O_{carb}$ (‰, VPDB). (b) $\delta^{13}C$ (‰, VPDB) versus $\delta^{18}O_{water}$ (‰, VSMOW). Error bars plotted for subplots A and B represent two standard error (2 s.e.) about the sample mean and unless visible, error bars are smaller than the datapoint. Error bars were omitted from subplots C and D for visual clarity and are reported in Figure 8 and Table S2. (c) $T(\Delta_{47})$estimates versus $\delta^{18}O_{carb}$ (‰, VPDB). (d) $T(\Delta_{47})$ estimates versus $\delta^{18}O_{water}$ (‰, VSMOW).

the lower lacustrine samples toward the Ely Limestone and Ely Spar $\delta^{13}C$ values and NCF and Ely Spar $\delta^{18}O_{carb}$ values, and the hotter $T(\Delta_{47})$ estimates suggest that they have been altered by hydrothermal fluids under varying *W/R* conditions. Some likely were altered by fluids under high *W/R* conditions (closer to the blue line in Figure 4) while others were under more intermediate *W/R* settings. In contrast, the $\delta^{18}O_{carb}$ values of the upper lacustrine samples cluster tightly around ∼−2‰, and as a result, they do not track a $\delta^{18}O_{water}$ contour, but rather fall closely along a $\delta^{18}O_{carb}$ contour (Figure 5c; Figure 1. The yellow star in both maps represents the approximate site of deposition of the NCF type section. (a) Reconstruction map of southern North America during the late Albian (∼105–102 Ma; modified from Blakey, 2020). Modeled seasonal prevailing wind directions are shown for Albian (∼100 Ma) winter (DJF: December, January, February) and summer (JJA: June, July, August) months with white arrows (Elder, 1988; Poulsen et al., 1999). Dark orange arrow shows approximate direction of subduction of the Farallon plate (DeCelles, 2004; DeCelles & Graham, 2015). The white box indicates the area of the map shown in (b) Regional tectonic map adapted from Di Fiori et al. (2020); Long, Henry, Muntean, Edmondo, and Cassel (2014), and Long, Henry, Muntean, Edmondo, and Thomas (2014). Gray shading shows the approximate spatial extents of Jurassic-Cretaceous deformational provinces of the North American Cordilleran mountain belt in western United States, while pink shading marks the Sierra Nevada magmatic arc (from Van Buer et al., 2009). All mapped NCF depositional basins are shown in purple (from Di Fiori et al., 2021).

**Table 3**
*Facies Averages Recalculated Excluding Samples Either Affected by Secondary Alteration (i.e., $Mb_{(lake)}$ and $Fc_{(lake)}$ Facies) or That Do Not Represent Ambient Environmental Conditions (e.g., $Mm_{(wetland)}$ Facies; See Section 5.3)*

| Setting | Facies | Median $\delta^{13}C$ (‰, VDPB) | Mean $\delta^{13}C$ (‰, VDPB) | $\delta^{13}C$ 2 s.e. | $\delta^{13}C$ maximum | $\delta^{13}C$ minimum | Median $\delta^{18}O_{carb}$ (‰, VDPB) | Mean $\delta^{18}O_{carb}$ (‰, VDPB) | $\delta^{18}O_{carb}$ 2 s.e. | $\delta^{18}O_{carb}$ maximum | $\delta^{18}O_{carb}$ minimum | *n* for $T(\Delta_{47})$ & $\delta^{18}O_{water}$ | Median $\delta^{18}O_{water}$ (‰, VDPB) | Mean $\delta^{18}O_{water}$ (‰, VDPB) | $\delta^{18}O_{water}$ 2 s.e. | $\delta^{18}O_{water}$ maximum | $\delta^{18}O_{water}$ minimum | Median $T(\Delta_{47})$ (°C) | Mean $T(\Delta_{47})$ (°C) | $T(\Delta_{47})$ 2s.e. | $T(\Delta_{47})$ maximum | $T(\Delta_{47})$ minimum |
|---|---|---|---|---|---|---|---|---|---|---|---|---|---|---|---|---|---|---|---|---|---|---|
| Palustrine | $Mp_{(wetland)}$ | −3.72 | −4.05 | 0.49 | −3.07 | −5.29 | −8.73 | −8.40 | 0.88 | −5.78 | −9.82 | 10 | −2.75 | −2.95 | 0.58 | −1.80 | −4.40 | 41.5 | 41.1 | 3.6 | 48.8 | 28.3 |
| Palustrine | $Mn_{(soil)}$ | −5.36 | −5.36 | 0.10 | −5.36 | −5.36 | −9.86 | −9.86 | 0.27 | −9.86 | −9.86 | 1 | −3.70 | −3.70 | 1.60 | −3.70 | −3.70 | 45.0 | 45.0 | 9.0 | 45.0 | 45.0 |
| Palustrine | $Mb_{(pond)}$ | −5.50 | −5.50 | 0.31 | −5.35 | −5.66 | −9.47 | −9.47 | 0.60 | −9.16 | −9.77 | 2 | −3.95 | −3.95 | 1.10 | −3.40 | −4.50 | 41.5 | 41.5 | 3.2 | 43.1 | 39.9 |
| Palustrine | $Gc_{(channel)}$ | −3.68 | −3.68 | 0.06 | −3.68 | −3.68 | −8.25 | −8.25 | 0.33 | −8.25 | −8.25 | 1 | −2.30 | −2.30 | 2.60 | −2.30 | −2.30 | 43.7 | 43.7 | 14.6 | 43.7 | 43.7 |
| Lacustrine | $M_{(lake)}$ | −3.62 | −3.44 | 0.46 | −1.99 | −4.30 | −2.31 | −2.26 | 0.22 | −1.37 | −2.73 | 14 | 2.65 | 2.62 | 0.50 | 3.90 | 1.00 | 39.2 | 37.8 | 2.5 | 43.5 | 29.1 |

*Note.* Recalculated facies averages are used to assess mid-Cretaceous paleoclimate conditions.

Additional differences between the upper and lower lacustrine samples become apparent when examining their $\delta^{13}C$ values. During primary deposition, the $\delta^{13}C$ of the dissolved inorganic carbon ($\delta^{13}C_{DIC}$) pool of lacustrine and palustrine systems is controlled by exchange of $CO_2$ between the atmosphere and water, the $\delta^{13}C$ of inflowing water and the atmosphere, and biological activity in the lake, such as photosynthesis, microbial respiration, and recycling of organic matter (Leng & Marshall, 2004; Talbot, 1990). If the upper and lower lacustrine samples both still preserve primary $\delta^{13}C$ values, we would expect to see relatively uniform $\delta^{13}C$ values because both facies would have drawn from the similar DIC pool in the lake, unless one facies experienced a greater influence of isotopic fractionation by biotic processes (e.g., Ingalls et al., 2020; Talbot, 1990). However, the upper lacustrine samples have more negative $\delta^{13}C$ values with much less spread (mean: −3.39‰ ± 0.44, 2 s.e.) than the lower lacustrine samples (mean: −1.55 ‰ ± 1.21, 2 s.e.). During alteration under high *W/R* conditions, a large volume of fluid can provide more carbon to the system that can isotopically exchange with the carbon of the affected rock. Signals of this isotopic exchange can be detected if the diagenetic fluid has a distinct $\delta^{13}C$ composition from the rock. This means that a higher *W/R* for fluids with $\delta^{13}C$ values that are distinct from the original rock will have a greater impact on $\delta^{13}C$ of the rock than that same fluid under low *W/R* exchange. The underlying marine limestones of the Carbon Ridge Formation and Ely Limestone were likely a substantial source for $^{13}C$-enriched $\delta^{13}C$ values in these diagenetic fluids and imprinted their isotopic signature in the lower lacustrine samples altered under relatively high *W/R* conditions.

Stratigraphically below the lacustrine unit of Stage 3 are a large stack of braided river conglomerates (Figure 2; Di Fiori et al., 2020; Fetrow et al., 2020). We posit that both the conglomerates and the contact between the conglomerate and lacustrine units may have provided a more porous conduit through which diagenetic fluids could migrate after lithification of the NCF, and it made the lower portion of the lacustrine unit more susceptible to diagenetic alteration. Alternatively, the biomicrite ($Mb_{(lake)}$) facies was more susceptible to diagenetic alteration due to the presence of fossil hash within the dense micrite matrix. Fossil hash could have increased the porosity of the facies, the crystal structure of the biogenic carbonate maybe be more susceptible to alteration, or a combination of the two. However, this facies-based explanation is highly speculative and is not supported by the presence of several $M_{(lake)}$ facies samples that also appear to be reset in the lower section of the lacustrine unit. Rather, the fact that all of the $M_{(lake)}$ facies samples that show similar signs of diagenesis are part of the lower lacustrine section, supports the hypothesis of stratigraphic control on diagenetic fluid migration for this part of the type section. This also explains the bigger temperature range and higher average temperature for the lower lacustrine section.

The isotopic and temperature patterns for upper lacustrine samples require a different explanation. The data from this section shows a tight trend along one $\delta^{18}O_{carb}$ contour, and although warm, these samples are some of the coolest NCF $T(\Delta_{47})$ estimates; $T(\Delta_{47})$ ranges from 29.1 to 43.5°C, with a mean of 37.8°C (±2.5, 2 s.e.; Table 3). One possible explanation is that they have experienced secondary alteration under low *W/R* conditions (like Scenario 2, orange line). While we cannot rule this out completely, given that the other data demonstrate the potential for alteration to higher temperatures, it seems unlikely that this suite of samples would not have a similarly high range of temperatures to the $Mb_{(lake)}$ facies.

We interpret that the upper lacustrine data reflect temperature control on the $\delta^{18}O_{water}$ at the time of deposition, with minimal influence of evaporation. For middle-to high-latitude regions in our modern climate system, mean annual $\delta^{18}O_{precip}$ values increase by 0.4–0.6‰ for every 1°C increase in MAT based on globally distributed data (Craig, 1965; Dansgaard, 1964; Rozanski et al., 1993). $\delta^{18}O_{precip}$/T slopes may have been smaller relative to the modern spatial relationship when past global climate states were warmer than present and when the relationship is based on temporal data sets of temperature and $\delta^{18}O_{water}$ rather than spatial data sets (Boyle, 1997; Fricke & O'Neil, 1999; Jouzel et al., 1997; Snell et al., 2013). For example, estimates of the temporal $\delta^{18}O_{precip}$ to temperature relationship from the Eocene Bighorn Basin, WY—another mid-latitude, North American, terrestrial sedimentary basin that also formed during greenhouse climate conditions—range from 0.32‰/°C (±0.10, 2 s.e.) (Snell et al., 2013) to 0.36–0.39‰/°C (Secord et al., 2010). The slope of $\delta^{18}O_{water}/T(\Delta_{47})$ for the upper lacustrine samples from the NCF is 0.18‰/°C (±0.68, 2 s.e.) and is consistent with an expected shallow

slope given the hothouse climate of the mid-Cretaceous. In addition, the NCF lacustrine system is interpreted as a balance-filled lake (as opposed to a closed-basin lake), which is supported by the lack of covariance in $\delta^{13}C$ and $\delta^{18}O_{carb}$ in the lacustrine facies that would be expect for a closed-basin, evaporation dominated lake (Figure 5a; Leng & Marshall, 2004; Li & Ku, 1997; Martin-Bello et al., 2019; Talbot, 1990). Together, the similarities of the $\delta^{18}O_{precip}/T(\Delta_{47})$ slopes between the mid-Cretaceous NCF and the Eocene Bighorn Basin, the limited range in $T(\Delta_{47})$ and the lack of signs of significant evaporation suggest that the upper lacustrine samples preserve primary $T(\Delta_{47})$ values (Figure 7) and reflect temperature-controlled $\delta^{18}O_{precip}$ rather than diagenesis.

#### 5.3.2. Lower NCF (~113–112 Ma)—Palustrine Facies

The lower NCF preserves complexly interbedded palustrine pebbly pelmicrite ($Mp_{(wetland)}$) and mottled micrite ($Mm_{(wetland)}$), pond biomicrite ($Mb_{(pond)}$), and paleosols with carbonate nodules ($Mn_{(soil)}$). The water depth gradient reflected by these facies implies differential effects of radiative heating of water and exposed sediment, pedogenesis, and inundation by nearby river channels on each facies, and provides a framework with which to explain the similarities and differences of these facies (Figure 3).

First, the overlap in $\delta^{13}C$ values of the palustrine facies indicates that they likely reflect a common DIC pool during carbonate precipitation (Figure 6a or 6b). The slightly lower $\delta^{13}C$ values of the mottled micrite compared to the pebbly pelmicrite may result from more frequent subaerial exposure and associated incipient pedogenesis. This would likely increase the amount of soil $CO_2$ in the DIC pool, driving $\delta^{13}C$ values lower (e.g., Ehleringer et al., 2000). Second, the palustrine facies show greater variability than the upper lacustrine samples and do not fall particularly along either the $\delta^{18}O_{carb}$ or the $\delta^{18}O_{water}$ contours (Figure 6c or 6d). This suggests that the palustrine facies did not undergo significant secondary alteration due to hydrothermal fluids, in contrast to the lower lacustrine samples. On the other hand, evidence of mud cracking and pseudo-microkarstification found in the palustrine facies (Fetrow et al., 2020) indicate that evaporation was an active process in the palustrine environment, plausibly generating the spread in the palustrine isotope data (Figure 6).

Third, the mottled micrite samples generally record hotter $T(\Delta_{47})$ than the pebbly pelmicrite. This pattern agrees well with the palustrine depositional model, where the mottled micrite that formed in shallower wetlands would have warmed more quickly with diurnal and seasonal temperature variations compared to wetland areas with deeper water. The $T(\Delta_{47})$ values as high as 68°C in the mottled micrite facies (average of 52°C; Table 2) may seem too high to be "reasonable" Earth surface temperatures, but this overlooks the extreme temperatures that are possible in certain depositional settings. The shallower palustrine environments represented by the mottled micrite facies were likely dark mudflats with sparse to no vegetation to provide shade (Fetrow et al., 2020). Studies of modern "bare-skin" surface temperatures—defined as the surface temperature that bare, un-vegetated ground can reach due to a combination of ambient air temperature and direct radiative heating—show that bare-skin temperatures can reach temperatures up to 70°C (158°F), 30–50°C hotter than air temperature, depending on the color of the exposed regolith and vegetative extent (Mildrexler et al., 2011) and surface sediment temperatures can vary up to ~28°C in one diurnal cycle on tidal flats (Cho et al., 2005). $T(\Delta_{47})$ records the temperature of mineral precipitation, and so have the potential to preserve hot bare-skin temperatures rather than average water or ground temperatures. The mottled micrite $T(\Delta_{47})$ values are all within the range of these modern surface temperature extremes, and so it is plausible that these hot temperatures do reflect primary conditions (Figure 7). Additionally, since carbonates are reversely soluble minerals, it is possible that more carbonate is produced during relatively short but very warm events, resulting in extreme temperatures being over-represented in a carbonate sample, relative to what a true temporal average of temperature was during sedimentation. A few ($n = 5$) samples of the pebbly pelmicrite facies preserve hot temperatures (>50°C) and $\delta^{18}O_{water}$ values that cluster with the mottled micrite facies (i.e., blue datapoints outside of black circle in Figure 6c or 6d). This may have resulted from some samples of the pebbly pelmicrite facies having experienced stronger radiative heating than others, causing this subset to preserve higher $T(\Delta_{47})$ estimates and more $^{18}O$-enriched $\delta^{18}O_{water}$ values. These samples provide an example of how carbonates in a palustrine environment form along a spectrum of depositional conditions (Figure 3).

Even if the samples from the mottled micrite facies are unaltered and their $T(\Delta_{47})$ values reflect bare-skin temperatures, the mottled micrite facies data should not used to interpret "ambient" regional climate or climatic trends through time. These data still provide some constraint on overall response of the environment to the climate of the time, however. For example, an environment that can experience extreme surface temperatures of 50–70°C will

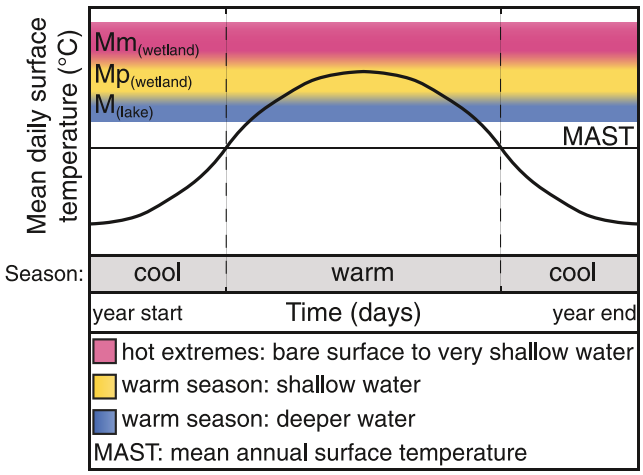


**Figure 7.** A schematic of mean daily surface temperatures (°C) throughout a year. Color shading demonstrates the temperature ranges that are likely captured by the Newark Canyon Formation (NCF) carbonate-bearing facies $M_{(lake)}$, $Mp_{(wetland)}$, and $Mm_{(wetland)}$. Note that the temperature ranges that are captured by each facies can overlap with another because the different facies can encode overlapping portions of surface temperature variability throughout a year.

impose, for even short amounts of time, restrictions on the flora and fauna that can survive in these settings. This may be one reason that the NCF palustrine carbonates show few signs of vegetative colonization; it would have been difficult for plants to persist if the shallow portions on the wetlands frequently dried up and experienced extreme warmth. This discussion highlights the difficulty of setting an upper $T(\Delta_{47})$ boundary below which all samples reflect ambient climate at the time of deposition.

The pebbly pelmicrite facies was deposited in deeper portions of the palustrine environment and does not preserve sedimentary features of extreme desiccation or subaerial exposure, unlike the mottled micrite. We expect, therefore, the pebbly pelmicrite facies to record temperatures closest to average warm-season conditions (Figure 7). With one exception, there are no palustrine samples with $T(\Delta_{47})$ estimates cooler than 35°C, and the pebbly pelmicrite samples have a weighted mean of 41.1°C (±3.6°C, 2 s.e.; Table 3). Therefore, we interpret that the lower temperature zone of 35–40°C as a reasonable estimate of the warm season water temperatures present on the landscape during the time of deposition of these palustrine carbonates.

## 6. Paleoclimate Implications

### 6.1. Comparison of NCF Temperatures to Other Records

New isotope averages and standard errors were calculated using only samples interpreted to preserve "ambient" surface conditions during time of deposition, excluding samples deemed to preserve environmental extremes (e.g., $Mm_{(wetland)}$ and small subset of $Mp_{(wetland)}$ facies) or evidence of secondary alteration (i.e., $Mb_{(lake)}$ and $Fc_{(lake)}$ facies) (Table 3 and Figure 8). The palustrine carbonate unit of the lower NCF type section (pebbly pelmicrite facies ($Mp_{(wetland)}$); ~113–112 Ma) and the upper portion of the balance-filled lacustrine unit (micrite facies ($M_{(lake)}$); ~112–103 Ma) preserve average warm season water temperatures of 41.1°C (±3.6°C, 2 s.e.) and 37.8°C (±2.5°C, 2 s.e.), respectively (Figure 8 and Table 3). These high temperatures from the mid-Cretaceous Sevier hinterland imply warm overall regional climate conditions and agree closely with a hot global climatic setting of the mid-Cretaceous just before the Cretaceous Thermal Maximum. While the temperatures recorded in the NCF at first glance seem extreme, they are similar or only slightly warmer than mid-Cretaceous sea surface and terrestrial temperature estimates, and for terrestrial records from other hothouse climate periods. For example, tropical sea surface temperature estimates derived from $TEX_{86}$ in Albian-Santonian (113–83 Ma) sediments in the western equatorial Atlantic indicate temperatures ranging from ~31 to 35°C (Forster et al., 2007). Oxygen isotopes and Mg/Ca ratios in Albian to Santonian (~113–83 Ma) planktonic foraminifera support upper ocean temperature estimates between 33 and 42°C for the tropical Atlantic (Bice et al., 2006). A simulation of Mid-Cretaceous global climate predicts an average warm season (JJA) surface temperature range for the Sevier hinterland region of 20–30°C, which likely represents a minimum estimate because the model assumes a single vegetation type and soil type (Barron et al., 1995). As discussed previously, $T(\Delta_{47})$ estimates from mid-Cretaceous Cedar Mountain Formation paleosol and palustrine carbonates span from 30 to 39°C, which closely overlaps with NCF $T(\Delta_{47})$ estimates (Ludvigson et al., 2010, 2015; M. B. Suarez et al., 2021). Like our samples, these temperatures likely represent carbonate formation during the warm season in addition to some amount of radiative heating.

Ultimately the mechanistic driver of carbonate formation in an environment will determine the season(s) during which the majority of carbonate is deposited. For example, increases in temperature or the additional influx of dissolved calcium into a system can increase the saturation state of calcium carbonate in an aqueous solution and result in carbonate precipitation (Zeebe & Wolf-Gladrow, 2001). While there is growing evidence that terrestrial carbonates form during either warm seasons and/or during seasons with episodic wetting/drying cycles as discussed previously, it is important to consider the paleoclimate implications if the temperature reconstructions from the NCF record a different portion of the year, such as the spring or fall. If we consider a scenario in which most of the carbonate in the NCF was not deposited in the warm season, it would imply that the mean average

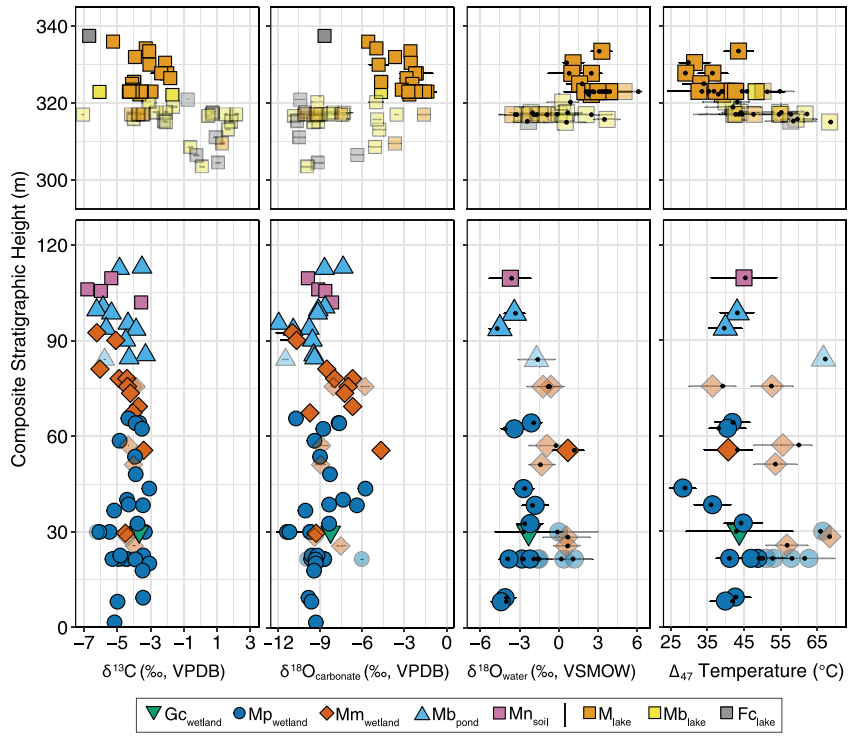


**Figure 8.** Weighted mean values for $\delta^{13}C$, $\delta^{18}O_{carb}$, $\delta^{18}O_{water}$, and $T(\Delta_{47})$ versus composite stratigraphic height for the Newark Canyon Formation (NCF) type section. Note the stratigraphic break between the lower and upper NCF units. Means are weighted by standard error for each sample replicate. Error bars represent two standard errors (2 s.e.) about the sample mean. Unless visible, error bars are smaller than the datapoint. For comparison, black dots in $\delta^{18}O_{water}$ and $\Delta_{47}$ temperature estimate panels represent the median value of the replicates analyzed for each sample. Partially transparent symbols were either affected by secondary alteration (i.e., $Mb_{(lake)}$ and $Fc_{(lake)}$ facies) or do not represent ambient environmental conditions (e.g., $Mm_{(wetland)}$ facies). Opaque symbols indicate samples used to assess mid-Cretaceous paleoclimate conditions.

temperature of the Sevier hinterland was even hotter than we interpret it to be in this study, regardless of driving precipitation mechanism.

It is also notable that these temperatures are similar to other records from times of hothouse climate. $T(\Delta_{47})$ values from paleosol carbonates from the Bighorn Basin (Wyoming, USA) have peak temperatures of ~40–42°C at the Paleocene-Eocene Thermal Maximum and just before the Early Eocene Climatic Optimum (EECO; Snell et al., 2013). In general, foraminiferal $\delta^{18}O$ compilations suggest similar temperature estimates for the mid-Cretaceous and Early Eocene (which represents the apex of Cenozoic warmth) and so the similarity in peak temperatures for these records is supported by the similarities in the marine records (B. T. Huber et al., 2018).

### 6.2. Implications for Hydroclimate

While $\delta^{18}O_{water}$ values estimated from $T(\Delta_{47})$ records can provide insights into the regional hydroclimate during the mid-Cretaceous, factors like moisture source, source water $\delta^{18}O$ and transport distance, and the extent of evaporative modification of $\delta^{18}O_{water}$ values will all impact $\delta^{18}O_{water}$ values of soils, wetlands, and lakes. There is significant uncertainty in paleo-wind directions and thus moisture sources for the western USA in the mid-Cretaceous. Climate modeling for North America at ~90 Ma (Turonian), which corresponds most closely with deposition of the upper NCF lacustrine unit, suggests that during the winter the western USA received westerly winds from the Pacific Ocean, while during the summer moisture came from the east, derived from the WIS (Elder, 1988; Poulsen et al., 1999). In contrast, this same study suggests significantly different paleowind directions, and thus moisture sources, for the western USA at ~100 Ma (Albian/Cenomanian). In the Albian/Cenomanian, winds in the winter blew from the southwest and delivered moisture from the Pacific Ocean while summer winds came from the north supplying moisture from either the Pacific or Arctic Oceans. These two times were substantially different in the western USA with respect to the degree of incursion of the WIS; 100 Ma

featured moderate encroachment of marine waters from the north into interior North America, which therefore increased the transport distance of moisture to the NCF depositional basin, while at 90 Ma the seaway was fully connected from north to south, which implies shorter transport distances if/when moisture sources came from the east of the site (Cobban & Gill, 1973; McDonough & Cross, 1991; Scott et al., 2018).

For the NCF location, moisture coming from the Gulf and/or Arctic during the Aptian/Albian traveled farther than moisture coming from the Pacific, while moisture coming from the Pacific may have encountered some topographic relief on its way to the NCF basin. Given that the degree of Rayleigh fractionation associated with transport of moisture is the net effect of temperature, transport distance, and elevation (among other effects, e.g., Rozanski et al., 1993), it is difficult to determine which moisture source would have been more $^{18}$O-depleted by the time it reached the basin. In addition, the high temperatures, summer bias, and high humidity of the time would have reduced the extent of fractionation due to transport (e.g., Poulsen & Jeffery, 2011; Rozanski et al., 1993). These combined effects could have created meteoric water that was minimally $^{18}$O-depleted at the NCF site relative to its marine source water, regardless of the specific moisture source. Model-predicted $\delta^{18}O_{water}$ estimates for Pacific Ocean surface water along the west coast of the North American continent at ~39°N in the mid-Cretaceous range from −2‰ to −0.5‰ (Zhou et al., 2008). If a Pacific Ocean-derived moisture source is assumed, then the average palustrine $\delta^{18}O_{water}$ for Stage 1 of −2.97‰ ±1.12 (2 s.e.) further supports minimal fractionation during moisture transport to the NCF depositional basin.

Due to the characteristics of the two distinct depositional settings (i.e., palustrine vs. lacustrine), the +5‰ shift between the average palustrine $\delta^{18}O_{water}$ for Stage 1 (−2.97‰ ±1.12‰, 2 s.e.) and the Stage 3 lacustrine average (+2.71‰ ±0.66, 2 s.e.) can most likely be explained by a change in dominant moisture source(s) to the NCF basin during its ~15 Myr depositional record (Figure 8). As discussed above, at the time of NCF Stage 3 deposition, the WIS had inundated the central North American continent and global climate was warmer than during Stage 1. Together, this could have caused both a seasonal shift in moisture sources to the NCF basin during this time (M. B. Suarez et al., 2011; Ufnar et al., 2002; White et al., 2001), and further reduced transport-related fractionation, resulting in higher $\delta^{18}O$ of meteoric water in the region. This is consistent with the shallow slope of our lake water $\delta^{18}O_{water}/T(\Delta_{47})$ relationship, and the other indications that this region was humid at the time (e.g., Hasegawa et al., 2012; Qiao et al., 2022).

## 7. Conclusions

We presented $\delta^{13}C$, $\delta^{18}O_{carb}$, $\delta^{18}O_{water}$, and $T(\Delta_{47})$ estimates for the NCF from central Nevada to examine terrestrial paleoclimate conditions of the Western USA during the mid-Cretaceous. Pairing our large stable isotope and $T(\Delta_{47})$ data set with a detailed depositional facies model provides an example of how paleoclimate and paleoenvironmental signals can be extracted from ancient and heterogeneous terrestrial carbonate archives. We use $\delta^{18}O_{carb}$–$\delta^{18}O_{water}$–$T(\Delta_{47})$ contour plots as endmember scenarios to deconvolve the influence of complex primary deposition from the effects of diagenetic processes. The estimated burial depth and peak temperatures of the NCF rule out significant solid-state reordering. The upper and lower portions of the lacustrine unit experienced differential fluid-mediated diagenesis, because of the stratigraphic proximity of the lower lacustrine section to more porous underlying conglomerate units. In contrast, the upper lacustrine unit may preserve primary temperatures and $\delta^{18}O_{water}$ values of catchment-integrated precipitation. The strong covariance of $\delta^{18}O_{water}$ with $T(\Delta_{47})$ for the upper lacustrine unit suggest that temperature is the dominant control on $\delta^{18}O_{precip}$ for this period of deposition.

We find that isotopic records from the palustrine facies preserved in the lower NCF type section reflect the heterogeneity of the complex environment in which they formed. The pebbly pelmicrite facies records temperatures closer to average ambient conditions that reflect warm season water temperatures of 35–40°C. In contrast, due to formation in shallow water, some of the mottled micrite facies record more extreme temperatures on the landscape (i.e., bare-skin temperatures). This facies demonstrates that even primary carbonates can record extremely high temperatures that are unaltered but not representative of ambient climate. For this reason, facies that capture extreme temperature conditions could be used to inform paleobotanical and paleoecological questions, such as habitability or temperature resiliency of specific species. Additionally, extreme conditions $T(\Delta_{47})$ estimates could be used to validate paleoclimate models that seek to estimate land surface temperatures, not just air temperatures. These findings are consistent with the general interpretation of the mid-Cretaceous as an extremely hot and humid time.

## Data Availability Statement

All raw and processed stable isotope data files, RStudio data processing scripts using software language R (R Core Team, 2022; Rstudio Team, 2020), corrected data spreadsheets, supplemental text, figures, and tables are available in an Open Science Framework repository (Fetrow et al., 2022). Stable isotope geochemistry data from different analytical sessions were compiled and averaged using an R script which is also available in the OSF repository and includes explanations for which sample replicate analyses were culled. This compilation R script includes all figures making code.

**Acknowledgments**
Field work and sample collection in Nevada was conducted on the unceded current and ancestral homelands of the Newe (Western Shoshone people). Laboratory work conducted at the University of Colorado Boulder was done on the unceded ancestral lands of the Ute, Cheyenne, and Arapaho peoples. This work was supported by a US National Science Foundation (NSF) grant awarded to KES (EAR-1524785), SPL (EAR-1524765), and JB (EAR-1524853), and an NSF Graduate Research Fellowship under Grant DGE-16501115 and a University of Colorado Boulder Geological Sciences Department Marcy and Bruce Benson Graduate Research Fellowship awarded to ACF. Any opinions, findings, and conclusions or recommendations expressed in this material are those of the author(s) and do not necessarily reflect the views of the National Science Foundation. The authors are grateful to Anna Todd and Kacey Connolly for their assistance and hard work in the field, and to Brett Davidheiser-Kroll for his support in the laboratory throughout this project. CUBES–SIL is a CU Boulder Core Facility associated with RRID: SCR_019300.

## References

Alonso-Zarza, A. M. (2003). Paleoenvironmental significance of palustrine carbonates and calcretes in the geological record. *Earth-Science Reviews*, *60*(3–4), 261–298. https://doi.org/10.1016/S0012-8252(02)00106-X

Alonso-Zarza, A. M., & Dorado-Valiño, M. (2006). A recent analog for palustrine carbonate environments: The Quaternary deposits of Las Tablas de Daimiel wetlands, Ciudad Real, Spain. In A. M. Alonso-Zarza, & L. H. Tanner (Eds.), *Paleoenvironmental record and applications of calcretes and palustrine carbonates* (pp. 153–168). https://doi.org/10.1130/2006.2416(10)

Alonso-Zarza, A. M., & Wright, V. P. (2010). Palustrine carbonates—Carbonates in continental settings: Facies, environments, and processes. In A. M. Alonso-Zarza, & L. H. Tanner (Eds.), *Carbonates in continental settings: Facies, environments, and processes* (pp. 103–131). Elsevier.

Anderson, N. T., Kelson, J. R., Kele, S., Da, M., Bonifacie, M., Horita, J., et al. (2021). A unified clumped isotope thermometer calibration (0.5°C–1,100°C) using carbonate-based standardization. *Geophysical Research Letters*, *48*, 1–22. https://doi.org/10.1029/2020gl092069

Andrzejewski, K., & Tabor, N. J. (2020). Paleoenvironmental and paleoclimatic reconstruction of Cretaceous (Aptian-Cenomanian) terrestrial formations of Texas and Oklahoma using phyllosilicates. *Paleogeography, Paleoclimatology, Paleoecology*, *543*, 109491. 10.1016/j.palaeo.2019.109491

Arenas-Abad, C., Vázquez-Urbez, M., Pardo-Tirapu, G., & Sancho-Marcén, C. (2010). Chapter 3: Fluvial and associated carbonate deposits. In *Carbonates in continental settings* (Vol. 61, pp. 133–175). Elsevier. 10.1016/S0070-4571(09)06103-2

Barron, E. J. (1983). A warm, equable Cretaceous: The nature of the problem. *Earth-Science Reviews*, *19*(4), 305–338. https://doi.org/10.1016/0012-8252(83)90001-6

Barron, E. J., Fawcett, P. J., Peterson, W. H., Pollard, D., & Thompson, S. L. (1995). A "simulation" of mid-Cretaceous climate. *Paleoceanography*, *10*(5), 953–962.

Barron, E. J., Fawcett, P. J., Pollard, D., & Thompson, S. (1993). Model simulations of the Cretaceous climates: Role of geography and carbon dioxide. *Philosophical Transactions of the Royal Society of London*, *341*, 307–316.

Barron, E. J., & Washington, W. M. (1982). Cretaceous climate: A comparison of atmospheric simulations with the geologic record. *Paleogeography, Paleoclimatology, Paleoecology*, *40*, 103–133. https://doi.org/10.1016/0031-0182(82)90086-4

Barron, E. J., & Washington, W. M. (1984). The role of geographic variables in explaining paleoclimates: Results from Cretaceous climate model sensitivity studies. *Journal of Geophysical Research*, *89*(D1), 1267–1279. https://doi.org/10.1029/JD089iD01p01267

Bergmann, K. D., Finnegan, S., Creel, R., Eiler, J. M., Hughes, N. C., Popov, L. E., & Fischer, W. W. (2018). A paired apatite and calcite clumped isotope thermometry approach to estimating Cambro-Ordovician seawater temperatures and isotopic composition. *Geochimica et Cosmochimica Acta*, *224*, 18–41. https://doi.org/10.1016/j.gca.2017.11.015

Bernasconi, S. M., Daëron, M., Bergmann, K. D., Bonifacie, M., Meckler, A. N., Affek, H. P., et al. (2021). InterCarb: A community effort to improve inter-laboratory standardization of the carbonate clumped isotope thermometer using carbonate standards. *Geochemistry, Geophysics, Geosystems*, *22*, 1–25. https://doi.org/10.1029/2020gc009588

Bice, K. L., Birgel, D., Meyers, P. A., Dahl, K. A., Hinrichs, K. U., & Norris, R. D. (2006). A multiple proxy and model study of Cretaceous upper ocean temperatures and atmospheric $CO_2$ concentrations. *Paleoceanography*, *21*(2), 1–17. https://doi.org/10.1029/2005PA001203

Blakey, D. (2020). DeepTimeMaps. deeptimemaps.com.

Bonde, J. W., Hilton, R. P., Jackson, F. D., & Druschke, P. A. (2015). Fauna of the Newark Canyon Formation (Lower Cretaceous), East-Central Nevada. In *Geological Society of Nevada 2015 Symposium, (April)* (pp. 139–150). Retrieved from https://www.researchgate.net/publication/275519952%0AFauna

Boyle, E. A. (1997). Cool tropical temperatures shift the global $\delta^{18}$O-T relationship: An explanation for the ice core $\delta^{18}$O-borehole temperature conflict? *Geophysical Research Letters*, *24*(3), 273–276.

Breecker, D. O., Sharp, Z. D., & McFadden, L. D. (2009). Seasonal bias in the formation and stable isotopic composition of pedogenic carbonate in modern soils from central New Mexico, USA. *The Geological Society of America Bulletin*, *121*(3/4), 630–640. Retrieved from http://gsabulletin.gsapubs.org/content/121/3-4/630.short

Brouwers, E. M., Clemens, W. A., Spicer, R. A., Ager, T. A., Carter, L. D., & Sliter, W. V. (1987). Dinosaurs on the North Slope, Alaska: High latitude, latest Cretaceous environments. *Science*, *237*(4822), 1608–1610. https://doi.org/10.1126/science.237.4822.1608

Burchfiel, B. C., Lipman, P. W., & Zoback, M. L. (1992). Introduction. In B. C. Burchfiel, P. W. Lipman, & M. L. Zoback (Eds.), *The Cordilleran orogen: Conterminous US* (pp. 1–6). Geological Society of America.

Burgener, L. K., Huntington, K. W., Hoke, G. D., Schauer, A., Ringham, M. C., Latorre, C., & Díaz, F. P. (2016). Variations in soil carbonate formation and seasonal bias over >4 km of relief in the western Andes (30°S) revealed by clumped isotope thermometry. *Earth and Planetary Science Letters*, *441*(C), 188–199. https://doi.org/10.1016/j.epsl.2016.02.033

Burgener, L. K., Huntington, K. W., Sletten, R., Watkins, J. M., Quade, J., & Hallet, B. (2018). Clumped isotope constraints on equilibrium carbonate formation and kinetic isotope effects in freezing soils. *Geochimica et Cosmochimica Acta*, *235*, 402–430. https://doi.org/10.1016/j.gca.2018.06.006

Case, J. A., Martin, J. E., Chaney, D. S., Reguero, M., Marenssi, S. A., Santillana, S. M., & Woodburne, M. O. (2000). The first duck-billed dinosaur (family *Hadrosauridae*) from Antarctica. *Journal of Vertebrate Paleontology*, *20*(3), 612–614. https://doi.org/10.1671/0272-4634(2000)020[0612:TFDBDF]2.0.CO;2

Chacko, T., Cole, D. R., & Horita, J. (2019). Equilibrium oxygen, hydrogen, and carbon isotope fractionation factors applicable to geologic systems. *Stable Isotope Geochemistry*, *43*(1977), 1–81.

Cho, Y. K., Kim, T. W., You, K. W., Park, L. H., Moon, H. T., Lee, S. H., & Youn, Y. H. (2005). Temporal and spatial variabilities in the sediment temperature on the Baeksu tidal flat, Korea. *Estuarine, Coastal and Shelf Science*, *65*(1–2), 302–308. https://doi.org/10.1016/j.ecss.2005.06.010

Cobban, W. A., & Gill, J. R. (1973). *Stratigraphy and geologic history of the Montana Group and equivalent rocks. Montana, Wyoming and North and South Dakota* (pp. 1–37). Geological Survey Professional Paper 776.

Coplen, T. B. (2011). Guidelines and recommended terms for expression of stable-isotope-ratio and gas-ratio measurement results. *Rapid Communications in Mass Spectrometry*, *25*(17), 2538–2560. https://doi.org/10.1002/rcm.5129

Craig, H. (1965). The measurement of oxygen isotope paleotemperatures. In E. Tongiorgi (Ed.), *Stable isotopes in oceanographic studies and paleotemperatures* (pp. 161–182).

Dansgaard, W. (1964). Stable isotopes in precipitation. *Tellus*, *16*(4), 436–468. Retrieved from http://tellusa.net/index.php/tellusa/article/view/8993

David, L. (1941). Leptolepis nevadensis, a New Cretaceous Fish. *Journal of Paleontology*, *15*(3), 318–321. Retrieved from https://www.jstor.org/stable/1298900

DeCelles, P. G. (2004). Late Jurassic to Eocene evolution of the Cordilleran thrust belt and foreland basin system, western USA. *American Journal of Science*, *304*(2), 105–168. https://doi.org/10.2475/ajs.304.2.105

DeCelles, P. G., & Coogan, J. C. (2006). Regional structure and kinematic history of the Sevier fold-and-thrust belt, central Utah. *The Geological Society of America Bulletin*, *118*(2006), 841–864. https://doi.org/10.1130/B25759.1

DeCelles, P. G., & Graham, S. A. (2015). Cyclical processes in the North American Cordilleran orogenic system. *Geology*, *43*(6), 499–502. https://doi.org/10.1130/G36482.1

Dee, S. G., Morrill, C., Kim, S. H., & Russell, J. M. (2021). Hot air, hot lakes, or both? Exploring Mid-Holocene African temperatures using proxy system modeling. *Journal of Geophysical Research: Atmospheres*, *126*(10), 1–23. https://doi.org/10.1029/2020JD033269

Dennis, K. J., Affek, H. P., Passey, B. H., Schrag, D. P., & Eiler, J. M. (2011). Defining an absolute reference frame for "clumped" isotope studies of $CO_2$. *Geochimica et Cosmochimica Acta*, *75*(22), 7117–7131. https://doi.org/10.1016/j.gca.2011.09.025

Dewey, J. F., & Bird, J. M. (1970). Mountain belts and new global tectonics. *Journal of Geophysical Research*, *75*(14), 2625–2647. https://doi.org/10.1029/JB075i014p02625

Dickinson, W. R. (2004). Evolution of the North American Cordillera. *Annual Review of Earth and Planetary Sciences*, *32*, 13–45. https://doi.org/10.1146/annurev.earth.32.101802.120257

Di Fiori, R. V., Long, S. P., Fetrow, A. C., Snell, K. E., Bonde, J. W., & Vervoort, J. D. (2020). Syn-contractional deposition of the Cretaceous Newark Canyon Formation, Diamond Mountains, Nevada: Implications for strain partitioning within the North American Cordillera. *Geosphere*, *16*, 1–21. https://doi.org/10.1130/abs/2019am-335173

Di Fiori, R. V., Long, S. P., Fetrow, A. C., Snell, K. E., Bonde, J. W., & Vervoort, J. D. (2021). The role of shortening in the Sevier Hinterland within the US. Cordilleran retroarc thrust system: Insights from the Cretaceous Newark Canyon Formation in Central Nevada. *Tectonics*, *40*, 1–31. https://doi.org/10.1029/2020TC006331

Druschke, P., Hanson, A. D., Wells, M. L., Gehrels, G. E., & Stockli, D. (2011). Paleogeographic isolation of the Cretaceous to Eocene Sevier hinterland, east-central Nevada: Insights from U-Pb and (U-Th)/He detrital zircon ages of hinterland strata. *The Geological Society of America Bulletin*, *123*(5–6), 1141–1160. https://doi.org/10.1130/B30029.1

Dunagan, S. P., & Driese, S. G. (1999). Control of terrestrial stabilization on Late Devonian palustrine carbonate deposition: Catskill Magnafacies, New York, USA. *Journal of Sedimentary Research*, *69*(1), 1–12. https://doi.org/10.1306/D4268A8B-2B26-11D7-8648000102C1865D

Ehleringer, J. R., Buchmann, N., & Flanagan, L. B. (2000). Carbon isotope ratios in below ground carbon cycle processes. *Ecological Applications*, *10*(2), 412–422. https://doi.org/10.1890/1051-0761(2000)010[0412:CIRIBC]2.0.CO;2

Eiler, J. M. (2007). Clumped-isotope" geochemistry-The study of naturally occurring, multiply-substituted isotopologues. *Earth and Planetary Science Letters*, *262*(3–4), 309–327. https://doi.org/10.1016/j.epsl.2007.08.020

Eiler, J. M. (2011). Paleoclimate reconstruction using carbonate clumped isotope thermometry. *Quaternary Science Reviews*, *30*(25–26), 3575–3588. https://doi.org/10.1016/j.quascirev.2011.09.001

Elder, W. P. (1988). Geometry of Upper Cretaceous bentonite beds: Implications about volcanic source areas and paleowind patterns, Western Interior, United States. *Geology*, *16*(9), 835–838. https://doi.org/10.1130/0091-7613(1988)016<0835:GOUCBB>2.3.CO;2

Fetrow, A. C., Snell, K. E., Di Fiori, R. V., Long, S. P., & Bonde, J. W. (2020). Early sevier orogenic deformation exerted principal control on changes in depositional environment recorded by the Cretaceous Newark Canyon Formation. *Journal of Sedimentary Research*, *90*, 1–22. https://doi.org/10.2110/jsr.2020.52

Fetrow, A. C., Snell, K. E., Di Fiori, R. V., Long, S. P., & Bonde, J. (2022). How hot is too hot? Disentangling Mid-Cretaceous Hothouse Paleoclimate From Diagenesis [Dataset]. OSF. Retrieved from https://osf.io/uwqzk/

Fluteau, F., Ramstein, G., Besse, J., Guiraud, R., & Masse, J. P. (2007). Impacts of paleogeography and sea level changes on Mid-Cretaceous climate. *Paleogeography, Paleoclimatology, Paleoecology*, *247*(3–4), 357–381. https://doi.org/10.1016/j.palaeo.2006.11.016

Folk, R. L. (1959). Practical petrographic classification of limestones. *Bulletin of the American Association of Petroleum Geologists*, *43*(1), 1–38. https://doi.org/10.1306/0BDA5C36-16BD-11D7-8645000102C1865D

Folk, R. L. (1962). Spectral subdivision of limestone types. In *Proceedings of the Symposium of the Association and the Society of Economic Paleontologists and Mineralogists*.

Föllmi, K. B. (2012). Early Cretaceous life, climate, and anoxia. *Cretaceous Research*, *35*(C), 230–257. https://doi.org/10.1016/j.cretres.2011.12.005

Forster, A., Schouten, S., Baas, M., & Sinninghe Damsté, J. S. (2007). Mid-Cretaceous (Albian-Santonian) sea surface temperature record of the tropical Atlantic Ocean. *Geology*, *35*(10), 919–922. https://doi.org/10.1130/G23874A.1

Fouch, T. D., Hanley, J. H., & Forester, R. M. (1979). Preliminary correlation of Cretaceous and Paleogene lacustrine and related nonmarine sedimentary and volcanic rocks in parts of the Eastern Great Basin of Nevada and Utah. In G. W. Newman, & H. D. Goode (Eds.), *Basin and Range Symposium and Great Basin Field Conference* (pp. 305–3012). Rocky Mountain Association of Petroleum Geologists and Utah Geological Association. Retrieved from http://archives.datapages.com/data/rmag/BasRanSym79/fouch.pdf

Freytet, P., & Verrecchia, E. P. (2002). Lacustrine and palustrine carbonate petrography: An overview. *Journal of Paleolimnology*, *27*, 221–237. https://doi.org/10.1023/A:1014263722766

Fricke, H. C., & O'Neil, J. R. (1999). The correlation between $^{18}O/^{16}O$ ratios of meteoric water and surface temperature its use in investigating terres. *Earth and Planetary Science Letters*, *170*, 181–196.

Gale, A. (2000). The Cretaceous World. In P. F. Culver, & S. J. Rawson (Eds.), *Biotic response to global change. The last 145 Myr* (pp. 4–19). Cambridge University Press. https://doi.org/10.1669/0883-1351(2004)019<0618:br>2.0.co;2

Gallagher, T. M., & Sheldon, N. D. (2016). Combining soil water balance and clumped isotopes to understand the nature and timing of pedogenic carbonate formation. *Chemical Geology*, *435*. https://doi.org/10.1016/j.chemgeo.2016.04.023

Ghosh, P., Garzione, C. N., & Eiler, J. M. (2006). Rapid uplift of the Altiplano revealed through $^{13}C$-$^{18}O$ bonds in paleosol carbonates. *Science*, *311*(5760), 511–515. https://doi.org/10.1126/science.1119365

Gierlowski-Kordesch, E. H. (2010). Lacustrine carbonate. In *Developments in sedimentology* (Vol. 61, pp. 1–101). Elsevier. https://doi.org/10.1016/S0070-4571(09)06101-9

Goldberg, S. L., Present, T. M., Finnegan, S., & Bergmann, K. D. (2021). A high-resolution record of early Paleozoic climate. *Proceedings of the National Academy of Sciences of the United States of America*, *118*(6). https://doi.org/10.1073/pnas.2013083118

Gonfiantini, R., Wassenaar, L. I., Araguas-Araguas, L., & Aggarwal, P. K. (2018). A unified Craig-Gordon isotope model of stable hydrogen and oxygen isotope fractionation during fresh or saltwater evaporation. *Geochimica et Cosmochimica Acta*, *235*, 224–236. https://doi.org/10.1016/j.gca.2018.05.020

Gröcke, D. R., Hesselbo, S. P., & Jenkyns, H. C. (1999). Carbon-isotope composition of Lower Cretaceous fossil wood: Ocean-atmosphere chemistry and relation to sea-level change. *Geology*, *27*(2), 155–158. https://doi.org/10.1130/0091-7613(1999)027<0155:CICOLC>2.3.CO;2

Harbeck, G. E. (1962). *A practical field technique for measuring reservoir evaporation utilizing mass-transfer theory* (Vol. 272-E, pp. 101–105). US Geological Survey Professional Paper. Retrieved from http://pubs.usgs.gov/pp/0272e/report.pdf

Hasegawa, H., Tada, R., Jiang, X., Suganuma, Y., Imsamut, S., Charusiri, P., et al. (2012). Drastic shrinking of the Hadley circulation during the mid-Cretaceous Supergreenhouse. *Climate of the Past*, *8*(4), 1323–1337. https://doi.org/10.5194/cp-8-1323-2012

Hay, W. W., De Conto, R. M., de Boer, P., Flögel, S., Song, Y., & Stepashko, A. (2018). Possible solutions to several enigmas of Cretaceous climate. *International Journal of Earth Sciences*, *108*, 587–620. https://doi.org/10.1007/s00531-018-1670-2

Held, I. M., & Soden, B. J. (2002). Water vapor feedback and global warming. *Annual Review of Energy and the Environment*, *25*(1), 441–475. https://doi.org/10.1146/annurev.energy.25.1.441

Held, I. M., & Soden, B. J. (2006). Robust responses of the hydrological cycle to global warming. *Journal of Climate*, *19*, 5686–5699. https://doi.org/10.1175/JCLI3990.1

Henkes, G. A., Passey, B. H., Grossman, E. L., Yancey, T. E., Shenton, B. J., Pe, A., et al. (2014). Temperature limits for preservation of primary calcite clumped isotope paleotemperatures. *Geochimica et Cosmochimica Acta*, *139*, 362–382. https://doi.org/10.1016/j.gca.2014.04.040

Hillhouse, J. W., & Grommé, S. (2011). Updated paleomagnetic pole from Cretaceous plutonic rocks of the Sierra Nevada, California: Tectonic displacement of the Sierra Nevada block. *Lithosphere*, *3*(4), 275–288. https://doi.org/10.1130/L142.1

Hough, B. G., Fan, M., & Passey, B. H. (2014). Calibration of the clumped isotope geothermometer in soil carbonate in Wyoming and Nebraska, USA: Implications for paleoelevation and paleoclimate reconstruction. *Earth and Planetary Science Letters*, *391*(C), 110–120. https://doi.org/10.1016/j.epsl.2014.01.008

Huber, B. T., Hodell, D. A., & Hamilton, C. P. (1995). Middle-late Cretaceous climate of the southern high latitudes: Stable isotopic evidence for minimal equator-to-pole thermal gradients. *The Geological Society of America Bulletin*, *107*(10), 1164–1191. https://doi.org/10.1130/0016-7606(1995)107<1164:MLCCOT>2.3.CO;2

Huber, B. T., MacLeod, K. G., Watkins, D. K., & Coffin, M. F. (2018). The rise and fall of the Cretaceous Hot Greenhouse climate. *Global and Planetary Change*, *167*, 1–23. https://doi.org/10.1016/j.gloplacha.2018.04.004

Huber, B. T., Norris, R. D., & MacLeod, K. G. (2002). Deep-sea paleotemperature record of extreme warmth during the Cretaceous. *Geology*, *30*(2), 123–126. https://doi.org/10.1130/0091-7613(2002)030<0123:DSPROE>2.0.CO;2

Huber, M. (2008). A hotter greenhouse? *Science*, *321*(5887), 353–354.

Huntington, K. W., Eiler, J. M., Affek, H. P., Guo, W., Bonifacie, M., Yeung, L. Y., et al. (2009). Methods and limitations of "clumped" $CO_2$ isotope ($\Delta_{47}$) analysis by gas-source isotope ratio mass spectrometry. *Journal of Mass Spectrometry*, *44*(9), 1318–1329. https://doi.org/10.1002/jms.1614

Huntington, K. W., Wernicke, B. P., & Eiler, J. M. (2010). Influence of climate change and uplift on Colorado Plateau paleotemperatures from carbonate clumped isotope thermometry. *Tectonics*. https://doi.org/10.1029/2009TC002449/full

Ingalls, M., Fetrow, A. C., Snell, K. E., Frantz, C. M., & Trower, E. J. (2022). Lake level controls the recurrence of giant stromatolite facies. *Sedimentology*, 1–26. https://doi.org/10.1111/sed.12967

Ingalls, M., Frantz, C. M., Snell, K. E., & Trower, E. J. (2020). Carbonate facies-specific stable isotope data record climate, hydrology, and microbial communities in Great Salt Lake, UT. *Geobiology*, *18*(5), 566–593. https://doi.org/10.1111/gbi.12386

Jenkyns, H. C. (2010). Geochemistry of oceanic anoxic events. *Geochemistry, Geophysics, Geosystems*, *11*(3), 1–30. https://doi.org/10.1029/2009GC002788

Jones, M. M., Petersen, S. V., & Curley, A. N. (2022). A tropically hot mid-Cretaceous North American Western Interior Seaway. *Geology*, *50*(8), 954–958. https://doi.org/10.1130/G49998.1

Jordan, T. E., & Allmendinger, R. W. (1986). The Sierra Pampeanas of Argentina: A modern analog of Rocky Mountain Foreland deformation. *American Journal of Science*, *286*, 737–764. https://doi.org/10.2475/ajs.286.10.737

Jouzel, J., Alley, R. B., Cuffey, K. M., Dansgaard, W., Grootes, P., Hoffmann, G., et al. (1997). Validity of the temperature reconstruction from water isotopes in ice cores. *Journal of Geophysical Research: Oceans*, *102*(C12), 26471–26487. https://doi.org/10.1029/97JC01283

Kelson, J. R., Huntington, K. W., Breecker, D. O., Burgener, L. K., Gallagher, T. M., Hoke, G. D., & Petersen, S. V. (2020). A proxy for all seasons? A synthesis of clumped isotope data from Holocene soil carbonates. *Quaternary Science Reviews*, *234*(106259), 1–18. https://doi.org/10.1016/j.quascirev.2020.106259

Kim, S.-T., & O'Neil, J. R. (1997). Equilibrium and nonequilibrium oxygen isotope effects in synthetic carbonates. *Geochimica et Cosmochimica Acta*, *61*(16), 3461–3475. https://doi.org/10.1016/S0016-7037(97)00169-5

Kopf, S., Davidheiser-Kroll, B., & Kocken, I. (2021). Isoreader: An R package to read stable isotope data files for reproducible research. *Journal of Open Source Software*, *6*(61), 2878. https://doi.org/10.21105/joss.02878

Leng, M. J., & Marshall, J. D. (2004). Paleoclimate interpretation of stable isotope data from lake sediment archives. *Quaternary Science Reviews*, *23*(7–8), 811–831. Retrieved from http://linkinghub.elsevier.com/retrieve/pii/S0277379104000101

Li, H. C., & Ku, T. L. (1997). $\delta^{13}C$-$\delta^{18}O$ covariance as a paleohydrological indicator for closed-basin lakes. *Paleogeography, Paleoclimatology, Paleoecology*, *133*(1–2), 69–80. https://doi.org/10.1016/S0031-0182(96)00153-8

Long, S. P. (2012). Magnitudes and spatial patterns of erosional exhumation in the Sevier hinterland, eastern Nevada and western Utah, USA: Insights from a Paleogene paleogeologic map. *Geosphere*, *8*, 881–901. https://doi.org/10.1130/GES00783.1

Long, S. P. (2015). An upper-crustal fold province in the hinterland of the Sevier orogenic belt, eastern Nevada, USA: A Cordilleran valley and ridge in the basin and range. *Geosphere*, *11*(2), 404–424. Retrieved from http://geosphere.gsapubs.org/content/11/2/404.full

Long, S. P. (2019). Geometry and extension magnitude of the Basin and Range Province (39°N), Utah, Nevada, and California, USA: Constraints from a province-scale cross-section. *The Geological Society of America Bulletin*, 1–21. https://doi.org/10.1130/B31974.1

Long, S. P., Henry, C. D., Muntean, J. L., Edmondo, G. P., & Cassel, E. J. (2014). Early Cretaceous construction of a structural culmination, Eureka, Nevada, USA: Implications for out-of-sequence deformation in the Sevier hinterland. *Geosphere*, *10*(3), 564–584. https://doi.org/10.1130/GES00997.1

Long, S. P., Henry, C. D., Muntean, J. L., Edmondo, G. P., & Thomas, R. D. (2014). *Preliminary geologic map of the southern Eureka Mining District, Eureka and White Pine counties, Nevada. Plate 1 of 2* (Vol. 1). Nevada Bureau of Mines and Geology, Nevada Geological Survey. Retrieved from http://publication/uuid/FE87EC43-D223-4AAF-9618-1FE7F4F836DE

Long, S. P., & Soignard, E. (2016). Shallow-crustal metamorphism during Late Cretaceous anatexis in the Sevier hinterland plateau: Peak temperature conditions from the Grant Range, eastern Nevada, USA. *Lithosphere*, *8*(2), 150–164. https://doi.org/10.1130/L501.1

Long, S. P., Thomson, S. N., Reiners, P. W., & Di Fiori, R. V. (2015). Synorogenic extension localized by upper-crustal thickening: An example from the Late Cretaceous Nevadaplano. *Geology*, *43*(4), 351–354. https://doi.org/10.1130/G36431.1

Ludvigson, G. A., Joeckel, R. M., Gonzalez, L. A., Gulbranson, E. L., Rasbury, E. T., Hunt, G. J., et al. (2010). Correlation of Aptian-Albian carbon isotope excursions in continental strata of the cretaceous Foreland Basin, Eastern Utah, USA. *Journal of Sedimentary Research*, *80*(11–12), 955–974. https://doi.org/10.2110/jsr.2010.086

Ludvigson, G. A., Joeckel, R. M., Murphy, L. R., Stockli, D. F., González, L. A., Suarez, C. A., et al. (2015). The emerging terrestrial record of Aptian-Albian global change. *Cretaceous Research*, *56*, 1–24. https://doi.org/10.1016/j.cretres.2014.11.008

Luz, B., Barkan, E., Yam, R., & Shemesh, A. (2009). Fractionation of oxygen and hydrogen isotopes in evaporating water. *Geochimica et Cosmochimica Acta*, *73*(22), 6697–6703. https://doi.org/10.1016/j.gca.2009.08.008

MacNeil, F. S. (1939). Fresh-water invertebrates and land plants of Cretaceous age from Eureka Nevada. *Journal of Paleontology*, *13*(3), 355–360. Retrieved from https://www.jstor.org/stable/1298743

Martin-Bello, L., Arenas, C., Andrews, J. E., Alonso-Zarza, A. M., & Marca, A. (2019). Lacustrine stromatolites as multi-scale recorders of climate change: Insights from the Miocene Ebro Basin. *Paleogeography, Paleoclimatology, Paleoecology*, *530*, 312–329. https://doi.org/10.1016/j.palaeo.2019.05.001

McDonough, K. J., & Cross, T. A. (1991). Late Cretaceous sea level from a paleoshoreline. *Journal of Geophysical Research*, *96*(B4), 6591–6607. https://doi.org/10.1029/91JB00281

Mildrexler, D. J., Zhao, M., & Running, S. W. (2011). Satellite finds highest land skin temperatures on Earth. *Bulletin of the American Meteorological Society*, *92*(7), 855–860. https://doi.org/10.1175/2011BAMS3067.1

Mintz, J. S., Driese, S. G., Breecker, D. O., & Ludvigson, G. A. (2011). Influence of changing hydrology on pedogenic calcite precipitation in vertisols, Dance Bayou, Brazoria County, Texas, USA: Implications for estimating paleoatmospheric $pCO_2$. *Journal of Sedimentary Research*, *81*(6), 394–400. https://doi.org/10.2110/jsr.2011.36

Nolan, T. B., & Hunt, R. N. (1962). The Eureka Mining District Nevada. https://doi.org/10.3133/pp406

Nolan, T. B., Merriam, C. W., & Blake, M. C. J. (1974). Geologic map of Pinto Summit Quadrangle, Eureka and White Pine Counties, Nevada, US Geological Survey Miscellaneous Investigations Series. Map I-793.

Nolan, T. B., Merriam, C. W., & Williams, J. S. (1956). *The stratigraphic section in the vicinity of Eureka, Nevada* (Vol. 276). Geological Survey Professional Paper. https://doi.org/10.3133/pp276

Olivero, E. B., Gasparini, Z., Rinaldi, C. A., & Scasso, R. A. (1991). First record of dinosaurs in Antarctica (Upper Cretaceous, James Ross Island): Paleogeographical implications. In M. R. A. Thomson, J. A. Crame, & J. W. Thomson (Eds.), *Geological evolution of Antarctica* (pp. 617–622). Cambridge University Press.

Pagani, M., Huber, M., & Sageman, B. (2013). Greenhouse climates. In *Treatise on geochemistry* (2nd ed., Vol. 6, pp. 281–304). Elsevier Ltd. https://doi.org/10.1016/B978-0-08-095975-7.01314-0

Pagel, M., Barbin, V., Blanc, P., & Ohnenstetter, D. (2000). *Cathodoluminescence in geosciences*. In M. Pagel, V. Barbin, P. Blanc, & D. Ohnenstetter (Eds.), Springer-Verlag.

Parrish, J. M., Parrish, J. T., Hutchison, J. H., & Spicer, R. A. (1987). Late Cretaceous vertebrate fossils from the North Slope of Alaska and implications for Dinosaur ecology. *PALAIOS*, *2*(4), 377–389.

Parrish, J. T., & Spicer, R. A. (1988). Late Cretaceous terrestrial vegetation: A near-polar temperature curve. *Geology*, *16*(1), 22–25. https://doi.org/10.1130/0091-7613(1988)016<0022:LCTVAN>2.3.CO;2

Passey, B. H., & Henkes, G. A. (2012). Carbonate clumped isotope bond reordering and geospeedometry. *Earth and Planetary Science Letters*, *351–352*, 223–236. https://doi.org/10.1016/j.epsl.2012.07.021

Passey, B. H., Levin, N. E., Cerling, T. E., Brown, F. H., & Eiler, J. M. (2010). High temperature environments of human evolution in East Africa based on bond ordering in paleosol carbonates. In *Proceedings of the National Academy of Sciences*. Retrieved from http://www.pnas.org/content/107/25/11245.short

Petersen, S. V., Defliese, W. F., Saenger, C., Daëron, M., Huntington, K. W., John, C. M., et al. (2019). Effects of improved $^{17}O$ correction on inter-laboratory agreement in clumped isotope calibrations, estimates of mineral-specific offsets, and acid fractionation factors. *Geochemistry, Geophysics, Geosystems*. https://doi.org/10.1029/2018GC008127

Platt, N. H. (1989). Lacustrine carbonates and pedogenesis: Sedimentology and origin of palustrine deposits from the Early Cretaceous Rupelo Formation, W. Cameros Basin, N Spain. *Sedimentology*, *36*(4), 665–684. https://doi.org/10.1111/j.1365-3091.1989.tb02092.x

Poulsen, C. J., Barron, E. J., Johnson, C. C., & Fawcett, P. (1999). *Links between major climatic factors and regional oceanic circulation in the mid-Cretaceous*. Geological Society Special Publication. Evolution (Special Paper 332).

Poulsen, C. J., & Jeffery, M. L. (2011). Climate change imprinting on stable isotopic compositions of high-elevation meteoric water cloaks past surface elevations of major orogens. *Geology*. Retrieved from http://geology.gsapubs.org/content/39/6/595.short

Qiao, D., Peng, N., Kuang, H., Liu, Y., Liu, Y., Cui, L., & Wang, Y. (2022). Changes in prevailing surface-paleowinds reveal the atmospheric circulation transition during Early Cretaceous in North China. *Paleogeography, Paleoclimatology, Paleoecology*, *586*, 110784. https://doi.org/10.1016/j.palaeo.2021.110784

Quade, J., Eiler, J., Daëron, M., & Achyuthan, H. (2013). The clumped isotope geothermometer in soil and paleosol carbonate. *Geochimica et Cosmochimica Acta*, *105*, 92–107. https://doi.org/10.1016/j.gca.2012.11.031

R Core Team (2022). R: A language and environment for statistical computing. R Foundation for Statistical Computing, Vienna, Austria (Version 3.6.3) [Software]. Retrieved from https://www.R-project.org/

Rich, T. H., Vickers-Rich, P., & Gangloff, R. A. (2002). Polar Dinosaurs. *Science*, *295*(5557), 979–981. https://doi.org/10.1126/science.1068920

Rozanski, K., Araguás Araguás, L., & Gonfiantini, R. (1993). Isotopic patterns in modern global precipation. In *Climate change in continental isotopic records* (Vol. 78). American Geophysical Union. Retrieved from http://www.agu.org/books/gm/v078/GM078p0001/GM078p0001.shtml

RStudio Team. (2020). RStudio: Integrated Development for R. RStudio, PBC, Boston, MA (Version 2022.2.3.492) [Software]. Rstudio Team. Retrieved from http://www.rstudio.com/

Ryb, U., Lloyd, M. K., & Eiler, J. M. (2021). Carbonate clumped isotope constraints on burial, uplift, and exhumation histories of the Colorado Plateau. *Earth and Planetary Science Letters*, *566*, 116964. https://doi.org/10.1016/j.epsl.2021.116964

Schauble, E. A., Ghosh, P., & Eiler, J. M. (2006). Preferential formation of $^{13}C$-$^{18}O$ bonds in carbonate minerals, estimated using first-principles lattice dynamics. *Geochimica et Cosmochimica Acta*, *70*(10), 2510–2529. https://doi.org/10.1016/j.gca.2006.02.011

Scott, R. W., Oboh-Ikuenobe, F. E., Benson, D. G., Holbrook, J. M., & Alnahwi, A. (2018). Cenomanian-Turonian flooding cycles: US Gulf Coast and Western Interior. *Cretaceous Research*, *89*, 191–210. https://doi.org/10.1016/j.cretres.2018.03.027

Secord, R., Gingerich, P. D., Lohmann, K. C., & MacLeod, K. G. (2010). Continental warming preceding the Paleocene-Eocene thermal maximum. *Nature*, *467*(7318), 955–958. https://doi.org/10.1038/nature09441

Smith, J. K., & Ketner, K. B. (1976). *Stratigraphy of post-Paleozoic rocks and summary of resources in the Carlin-Pinon Range area, Nevada, with a section on aeromagnetic survey*. Geological Survey Professional Paper. https://doi.org/10.3133/pp867B

Snell, K. E., Thrasher, B. L., Eiler, J. M., Koch, P. L., Sloan, L. C., & Tabor, N. J. (2013). Hot summers in the Bighorn Basin during the early Paleogene. *Geology*, *41*(1), 55–58. https://doi.org/10.1130/G33567.1

Strawson, F. M. (1981). *The geology of the Permian Carbon Ridge Formation*. University of Nevada Reno. Retrieved from https://scholarworks.unr.edu/handle/11714/1732

Suarez, C. A., González, L. A., Ludvigson, G. A., Kirkland, J. I., Cifelli, R. L., & Kohn, M. J. (2014). Multi-taxa isotopic investigation of paleohydrology in the lower Cretaceous Cedar Mountain Formation, Eastern Utah, USA: Deciphering effects of the Nevadaplano plateau on regional climate. *Journal of Sedimentary Research*, *84*(11), 975–987. https://doi.org/10.2110/jsr.2014.76

Suarez, M. B., González, L. A., & Ludvigson, G. A. (2011). Quantification of a greenhouse hydrologic cycle from equatorial to polar latitudes: The mid-Cretaceous water bearer revisited. *Paleogeography, Paleoclimatology, Paleoecology*, *307*(1–4), 301–312. https://doi.org/10.1016/j.palaeo.2011.05.027

Suarez, M. B., Knight, J. A., Godet, A., Ludvigson, G. A., Snell, K. E., Murphy, L., & Kirkland, J. I. (2021). Multiproxy strategy for determining paleoclimate parameters in the Ruby Ranch member of the Cedar Mountain Formation. *Geological Society Special Publication*, *507*(1), 313–334. https://doi.org/10.1144/SP507-2020-85

Takashima, R., Nishi, H., Huber, B. T., & Leckie, R. M. (2006). Greenhouse World and the Mesozoic Ocean. *Oceanography*, *19*(4), 64–74. https://doi.org/10.5670/oceanog.2006.07

Talbot, M. R. (1990). A review of the paleohydrological interpretation of carbon and oxygen isotopic ratios in primary lacustrine carbonates. *Chemical Geology: Isotope Geoscience section*, *80*(4), 261–279. https://doi.org/10.1016/0168-9622(90)90009-2

Tarduno, J. A., Brinkman, D. B., Renne, P. R., Cottrell, R. D., Scher, H., & Castillo, P. (1998). Evidence for extreme climatic warmth from Late Cretaceous Arctic vertebrates. *Science*, *282*(5397), 2241–2244. https://doi.org/10.1126/science.282.5397.2241

Ufnar, D. F., González, L. A., Ludvigson, G. A., Brenner, R. L., & Witzke, B. J. (2002). The mid-Cretaceous water bearer: Isotope mass balance quantification of the Albian hydrologic cycle. *Paleogeography, Paleoclimatology, Paleoecology*, *188*(1–2), 51–71. https://doi.org/10.1016/S0031-0182(02)00530-8

Ufnar, D. F., González, L. A., Ludvigson, G. A., Brenner, R. L., & Witzke, B. J. (2004). Evidence for increased latent heat transport during the Cretaceous (Albian) greenhouse warming. *Geology*, *32*(12), 1049–1052. https://doi.org/10.1130/G20828.1

Ufnar, D. F., Ludvigson, G. A., González, L., & Gröcke, D. R. (2008). Precipitation rates and atmospheric heat transport during the Cenomanian greenhouse warming in North America: Estimates from a stable isotope mass-balance model. *Paleogeography, Paleoclimatology, Paleoecology*, *266*(1–2), 28–38. https://doi.org/10.1016/j.palaeo.2008.03.033

Van Buer, N. J., Miller, E. L., & Dumitru, T. A. (2009). Early Tertiary paleogeologic map of the northern Sierra Nevada batholith and the northwestern Basin and Range. *Geology*, *37*(4), 371–374. https://doi.org/10.1130/G25448A.1

Vandervoort, D. S. (1987). *Sedimentology, provenance, and tectonic implications of the Cretaceous Newark Canyon Formation*. Montana State University. Retrieved from https://scholarworks.montana.edu/xmlui/bitstream/handle/1/7006/31762101234084.pdf?sequence=1

Vandervoort, D. S., & Schmitt, J. G. (1990). Cretaceous to early Tertiary paleogeography in the hinterland of the Sevier thrust belt, east-central Nevada. *Geology*, *18*, 567–570. https://doi.org/10.1130/0091-7613(1990)018<0567:CTETPI>2.3.CO;2

Voigt, S., Gale, A. S., & Voigt, T. (2006). Sea-level change, carbon cycling, and paleoclimate during the Late Cenomanian of northwest Europe; an integrated paleoenvironmental analysis. *Cretaceous Research*, *27*(6), 836–858. https://doi.org/10.1016/j.cretres.2006.04.005

Wells, M. L., Hoisch, T. D., Cruz-Uribe, A. M., & Vervoort, J. D. (2012). Geodynamics of synconvergent extension and tectonic mode switching: Constraints from the Sevier-Laramide orogen. *Tectonics*, *31*(1), 1–20. https://doi.org/10.1029/2011TC002913

Wendler, J. E., & Wendler, I. (2016). What drove sea-level fluctuations during the mid-Cretaceous greenhouse climate? *Paleogeography, Paleoclimatology, Paleoecology*, *441*, 412–419. https://doi.org/10.1016/j.palaeo.2015.08.029

White, T., González, L., Ludvigson, G., & Poulsen, C. (2001). Middle Cretaceous greenhouse hydrologic cycle of North America. *Geology*, *29*(4), 363–366. https://doi.org/10.1130/0091-7613(2001)029<0363:MCGHCO>2.0.CO;2

Wright, V. P., & Peeters, C. (1989). Origins of some Early Carboniferous calcrete fabrics revealed by cathodoluminescence: Implications for interpreting the sites of calcrete formation. *Sedimentary Geology*, *65*, 345–353. https://doi.org/10.1016/0037-0738(89)90033-X

Yonkee, W. A., & Weil, A. B. (2015). Tectonic evolution of the Sevier and Laramide belts within the North American Cordillera orogenic system. *Earth-Science Reviews*, *150*, 531–593. https://doi.org/10.1016/j.earscirev.2015.08.001

Zamanian, K., Pustovoytov, K., & Kuzyakov, Y. (2016). Pedogenic carbonates: Forms and formation processes. *Earth-Science Reviews*, *157*, 1–17. https://doi.org/10.1016/j.earscirev.2016.03.003

Zeebe, R. E., & Wolf-Gladrow, D. (2001). *$CO_2$ in seawater: Equilibrium, kinetics, isotopes (No. 65)*. Gulf Professional Publishing.

Zhou, J., Poulsen, C. J., Pollard, D., & White, T. S. (2008). Simulation of modern and middle Cretaceous marine $\delta^{18}O$ with an ocean-atmosphere general circulation model. *Paleoceanography*, *23*(3), 1–11. https://doi.org/10.1029/2008PA001596

Zuza, A. V., Levy, D. A., Mulligan, S., Zuzu, A. V., Levy, D. A., & Mulligan, S. (2020). Geologic field evidence for non-lithostatic overpressure recorded in the North American Cordillera hinterland, northeast Nevada. *Geosciences Frontier*, *95*(14), 106408. https://doi.org/10.1016/j.gsf.2020.10.006

## References From the Supporting Information

Alonso-Zarza, A. M., Genise, J. F., & Verde, M. (2011). Sedimentology, diagenesis, and ichnology of Cretaceous and Paleogene calcretes and palustrine carbonates from Uruguay. *Sedimentary Geology*, *236*(1–2), 45–61. https://doi.org/10.1016/j.sedgeo.2010.12.003

Alonso-Zarza, A. M., Meléndez, A., Martín-García, R., Herrero, M. J., & Martín-Pérez, A. (2012). Discriminating between tectonism and climate signatures in palustrine deposits: Lessons from the Miocene of the Teruel Graben, NE Spain. *Earth-Science Reviews*, *113*(3–4), 141–160. https://doi.org/10.1016/j.earscirev.2012.03.011

Carroll, A. R., & Bohacs, K. M. (1999). Stratigraphic classification of ancient lakes: Balancing tectonic and climatic controls. *Geology*, *27*(2), 99–102. https://doi.org/10.1130/0091-7613(1999)027<0099:SCOALB>2.3.CO;2

Cowardin, L. M., Carter, V., Golet, F. C., & LaRoe, E. T. (1979). *Classification of wetlands and deepwater habitats of the United States*. US Department of Interior, Fish and Wildlife Service. FWS/OBS-79/31.

Flugel, E. (2004). *Microfacies of carbonate rocks: Analysis, interpretation and application* (2nd ed.). Springer International Publishing. https://doi.org/10.1007/10.1007/978-3-642-03796-2

Freytet, P., & Plaziat, J. C. (1982). Continental carbonate sedimentation and pedogenesis—Late Cretaceous and Early Tertiary of Southern France. In H. Fuchtbauer, A. P. Lisitzyn, J. D. Milliman, & E. Seibold (Eds.), *Contributions to sedimentology* (Vol. 68–99, pp. 26–31).

Gray, M. B., & Nickelsen, R. P. (1989). Pedogenic slickensides, indicators of strain and deformation processes in redbed sequences of the Appalachian foreland. *Geology*, *17*(1), 72–75. https://doi.org/10.1130/0091-7613(1989)017<0072:PSIOSA>2.3.CO;2

Kraus, M. J. (1999). Paleosols in clastic sedimentary rocks: Their geologic applications. *Earth-Science Reviews*, *47*(1–2), 41–70. https://doi.org/10.1016/S0012-8252(99)00026-4

Mack, G. H., James, W. C., & Monger, H. C. (1993). Classification of paleosols. *The Geological Society of America Bulletin*, *105*(2), 129–136. https://doi.org/10.1130/0016-7606(1993)105<0129:COP>2.3.CO;2

Makaske, B. (2001). Anastomosing rivers: A review of their classification, origin, and sedimentary products. *Earth-Science Reviews*, *53*, 149–196. https://doi.org/10.1016/S0012-8252(00)00038-6

Marty, D., & Meyer, C. A. (2006). Depositional conditions of carbonate-dominated palustrine sedimentation around the K-T boundary (Faciès Rognacien, northeastern Pyrenean foreland, southwestern France). In A. M. Alonso-Zarza, & L. H. Tanner (Eds.), *Paleoenvironmental record and applications of calcretes and palustrine carbonates* (Special Pa, Vol. 416, pp. 169–187). Geological Society of America. https://doi.org/10.1130/SPE416

Murru, M., Ferrara, C., & Matteucci, R. (2015). Paleocene palustrine and ephemeral alluvial facies in southern Sardinia (Italy). *Italian Journal of Geosciences*, *134*(1), 134–148. https://doi.org/10.3301/IJG.2014.32

Nadon, G. C. (1994). The genesis and recognition of anastomosed fluvial deposits: Data from the St. Mary River Formation, Southwestern Alberta, Canada. *Journal of Sedimentary Research*, *B64*(4), 451–463. https://doi.org/10.1306/D4267FE1-2B26-11D7-8648000102C1865D

Tucker, M. E., & Wright, V. P. (1990). *Carbonate sedimentology*. Blackwell Publishing Ltd. https://doi.org/10.1002/9781444314175

Wright, V. P., & Platt, N. H. (1995). Seasonal wetland carbonate sequences and dynamic catenas: A re-appraisal of palustrine limestones. *Sedimentary Geology*, *99*, 65–71. https://doi.org/10.1016/0037-0738(95)00080-R